

Large Eddy Simulation of the IEA 15-MW Wind Turbine Using a Two-Way Coupled Fluid-Structure Interaction Model

Claudio Bernardi¹, Stefania Cherubini¹, Felice Manganeli¹, Giacomo Della Posta², Stefano Leonardi³, and Pietro De Palma¹

¹Department of Mechanics, Mathematics and Management, Polytechnic University of Bari, 70126, Bari, Italy (claudio.bernardi@poliba.it, stefania.cherubini@poliba.it, f.manganeli@phd.poliba.it, pietro.depalma@poliba.it)

²Department of Mechanical and Aerospace Engineering, Sapienza University of Rome, Rome, RM, 00184, Italy (giacomo.dellaposta@uniroma1.it)

³Department of Mechanical Engineering, University of Texas at Dallas, Richardson, TX, 75080, USA (stefano.leonardi@utdallas.edu)

Correspondence: Claudio Bernardi (claudio.bernardi@poliba.it)

Abstract

The aim of the work is studying the aeroelastic response of the IEA 15 MW Reference Wind Turbine (RWT) large-scale wind turbine using a high-fidelity fluid-structure interaction solver that combines large-eddy simulation with a modal computational structural dynamics solver through a two-way coupling. The fluid solver employs the actuator line model to simulate the interaction between the turbine blades and the fluid and the immersed boundary method to model the presence of the tower and nacelle. The results are compared with those obtained by the OpenFAST software, which is a well-known numerical tool for engineering predictions. A series of simulations have been performed with and without the presence of the tower and nacelle to better understand the effects of these components on flow structures and structural deformations. The largest discrepancies among the solvers have been observed in correspondence with the blade passage in front of the tower, which induces an abrupt alteration in the local incidence angle of the flow. Moreover, by comparing the outcomes of different structural approximations, it has been established that taking into account the torsional degree of freedom considerably affects the deformations, aerodynamic loads and power coefficient. Whereas, the nonlinearity of the solver appears to have a weak effect on the same quantities.

30 **Keywords**

31 Aeroelasticity, Large Eddy Simulation, Actuator Line Model, Fluid-Structure Interaction, Computa-
32 tional Fluid Dynamics, Computational Structural Dynamics, Blade Element Momentum, IEA-15MW
33 Wind Turbine.

34 **1 Introduction**

35 Wind energy has become a crucial component of the global transition toward renewable energy sources.
36 The increasing demand for clean energy has led to the development of large-scale wind turbines, such
37 as the IEA 15-MW offshore wind turbine developed within IEA Wind Task 37 (Gaertner et al., 2020a).
38 This turbine, with a rotor diameter of 240 meters and blades measuring 117 meters in length, rep-
39 represents a new frontier in wind energy technology (Gaertner et al., 2020b), and research is currently
40 pointing towards even larger rotors, reaching 22-MW of power production (Zahle et al., 2024). The
41 increasing scale and flexibility of such newly designed turbines present significant engineering chal-
42 lenges, particularly in predicting their aeroelastic response (Burton et al., 2011; Zheng et al., 2023).
43 As turbines grow in size, their structural components, especially the blades, are subject to complex
44 aerodynamic forces that cause deformations, which in turn affect the aerodynamic loads. Understand-
45 ing these interactions is essential to improve the performance, reliability, and longevity of large-scale
46 wind turbines (Manwell et al., 2010). In the worst cases, aeroelastic instabilities such as edgewise
47 instability and flutter might even lead to blade damage, as reported for the Lunderskov Mobelfabrik
48 19 m wind turbine blades (Moeller, 1997), with devastating effects on the turbine performance.

49 Aeroelasticity is critical in the design and analysis of modern wind turbines. Aeroelastic phenomena
50 such as dynamic stall, flutter, and their effects on fatigue loadings can have significant effects on tur-
51 bine performance, particularly as the blade length increases (Hansen, 2007). These blades experience
52 varying aerodynamic forces along their span, which can lead to substantial deformations. When blades
53 deform, they alter the local flow field, which in turn modifies the aerodynamic loads acting on them.
54 This feedback loop between aerodynamic forces and structural deformation makes it very difficult
55 to predict modern large-scale turbine performance under real-world operating conditions (Vermeer
56 et al., 2003; Wang et al., 2016a). Accurate evaluation of these interactions is key for ensuring turbine
57 efficiency and structural integrity, especially in offshore environments where wind conditions are more
58 severe (Bayati et al., 2017).

59 The numerical modeling of the blades in most of the numerical aeroelastic codes used nowadays
60 (Schepers et al., 2021) is accomplished by the Blade Element Momentum (BEM) model, due to its
61 robustness and low computational cost. It has been shown in the framework of the IEA WIND Task
62 47 Boorsma et al. (2023, 2024) that, if properly tuned, BEM can be a valuable engineering-type solver,
63 complementary to higher fidelity ones which have also higher computational costs. However, BEM
64 has still some limitations, since it relies on simplifying assumptions made on the impinging flow, such
65 as models of dynamic stall, dynamic inflow, yaw and tilt flows, and corrections of the aerofoil data for
66 taking into account three-dimensional effects and tip losses. More computationally expensive models
67 exist, such as panel methods and in general potential flow solvers and/or free-vortex wake methods, as
68 well as the actuator disc methods. Panel and free-wake vortex methods are able to capture unsteady

69 blade/rotor aerodynamics with good accuracy in different operating conditions (including off-design)
70 whenever massive flow separation phenomena do not occur Boorsma et al. (2018); Ribeiro et al. (2023).
71 However, those models need reference high-fidelity data in order to refine and/or assess the reliability
72 of these lower fidelity models. Therefore, the application of computational fluid dynamics (CFD) to
73 full-scale turbines is needed as a reference for describing the complex aerodynamics of the flow field
74 accurately (Sørensen, 2011), although for a limited number of flow case due to its high computational
75 cost.

76 However, coupling three-dimensional CFD simulations with computational structural dynamics (CSD)
77 solvers taking into account the deformation of the blade is not trivial. Three-dimensional structural
78 finite-element models are in fact able to fully describe the complex shape of a wind turbine blade but,
79 although accurate, these models are computationally expensive and hard to implement, leading to
80 only a few examples of coupling with CFD codes (Bazilevs et al., 2011; Yu and Kwon, 2014). Since
81 wind turbine blades are slender structures, their structural modeling can be more easily achieved using
82 beam models, where the blade is discretized as a series of one-dimensional beam elements, each char-
83 acterised by a given cross-sectional stiffness and mass per unit length. One-dimensional beam models
84 can be either modal, since natural frequencies and mode shapes of a turbine are directly related to the
85 natural frequencies of its blades, or they can rely on the geometrically exact beam theory including
86 non-linear effects (Sabale and Gopal, 2019).

87 Due to their ability to provide a rapid evaluation of the turbine performance, numerical tools based
88 on the BEM approach equipped with aeroelastic modules based on one-dimensional beam models,
89 are currently widespread (Schepers et al., 2021). A notable example is OpenFAST, a numerical code
90 developed at NREL (Jonkman, 2013) and widely used for aeroelastic simulations, which employs BEM
91 theory for aerodynamic modeling and various structural solvers, such as ElastoDyn (Damiani et al.,
92 2015) and BeamDyn (Wang et al., 2016b), for structural deformation analysis. However, it is still
93 not clear whether the predictions of such lifting-line aeroelastic codes are sufficiently accurate for
94 large-scale turbines, in which the effect of shear and inflow turbulence can lead to complex inflows and
95 turbine aerodynamic responses. Comparing the predictions of OpenFAST with those of a Large-Eddy
96 Simulation (LES) equipped with a structural one-dimensional beam model has shown that, for an
97 NREL 5MW wind turbine, the passage in front of the tower leads to large deformations which are
98 largely underestimated by OpenFAST (Bernardi et al., 2023).

99 Concerning rotors of even larger size, such as the IEA 15-MW reference turbine, it is not yet known
100 whether these discrepancies in the predictions of lifting-line codes with respect to CFD are even more
101 consistent. Using the unsteady Reynolds-Averaged Navier-Stokes (URANS) equations coupled with
102 an aeroelastic module, as reported by Pagamonci et al. (2023), has shown that neglecting the flexibility
103 of the blades in numerical simulations leads to an underestimation of the rotor thrust of approximately
104 2.5% for the IEA 15-MW turbine, which is not observed for the smaller NREL 5MW rotor. More-
105 over, this work also concluded that the deformation of long, slender blades may act as a filter for the
106 high-frequency fluctuations arising from the flow field, proving that taking into account the blades'
107 aeroelasticity in the design process of these machines is key for the future upscaling of turbine rotors.
108 Furthermore, Trigaux et al. (2024) observed how the use of high-fidelity aerodynamic models is crucial
109 to predict the aeroelastic effects of large rotors. These results suggest the need to investigate this issue
110 resorting to LES, which is capable of describing the dynamics of the flow more accurately.

111 In this context, the present work aims at studying the aeroelastic response of a large-scale 15-MW
112 wind turbine tower/nacelle assembly, resorting to both high-fidelity and engineering-fidelity computa-
113 tions. The investigation is conducted mainly by means of LES, whose results are compared with those
114 obtained by simpler and less computationally expensive models, such as the OpenFAST code. Com-
115 putations are performed by an in-house LES code using the immersed boundary method to model the
116 tower and nacelle and the Actuator Line Model (ALM) for blade modeling, coupled with a structural
117 modal solver, originally developed by Della Posta et al. (2022).

118 The discussion of the results highlights the role of the tower and nacelle in the dynamics of the aerody-
119 namical forces, thrust and power coefficients, as well as in the distribution of turbulent kinetic energy
120 within the wake, which could have an impact on the aerodynamic loads of downstream turbines in
121 wind farms. Moreover, the effect of the torsional degree of freedom has been investigated by comparing
122 the outcomes of different structural approximations.

123 The work is structured as follows. In section 2, the aerodynamic and structural solvers of both CFD-
124 CSD and OpenFAST codes are described in detail. In section 3, the numerical setup is presented. In
125 section 4, relevant results are discussed, and conclusions are drawn in section 5.

126 **2 Methodologies**

127 **2.1 CFD-CSD solver**

128 **2.1.1 Flow solver**

129 The simulations of the flow around the wind turbine are carried out through Large-Eddy Simulations
130 (LESs) of the incompressible, filtered, 3D Navier-Stokes equations, employing the in-house UTD-WF
131 solver introduced by Santoni et al. (2015). The UTD-WF framework has been progressively devel-
132 oped by Santoni et al. (2017, 2020) and further extended by Della Posta et al. (2022, 2023), where the
133 aeroelastic solver and the Leishman–Beddoes dynamic stall model were implemented. The solver has
134 been validated in its non-aeroelastic version by Santoni et al. (2017) against wind-tunnel data repro-
135 ducing the NTNU “Blind Test” and comparing simulations to Krogstad et al. (2015) measurements,
136 also considering the impact of tower and nacelle. Whereas, the recently developed version of the code
137 including the two-way FSI coupling Della Posta et al. (2023) has been validated through comparison
138 against reference datasets, including HAWC2-based results reported by Heinz (2013). The IEA 15MW
139 wind turbine configuration considered here has been cross-validated with many other aeroelastic nu-
140 merical codes in the International Energy Agency (IEA) Wind TCP Task 47 (Cacciola et al., 2025),
141 also considering turbulent inflow conditions (Schepers et al., 2025). Notice that prior validations by
142 Della Posta et al. (2022) of the CFD-CSD solver were made on a laminar uniform and a turbulent
143 sheared inflows for a 5 MW NREL turbine, whereas our study extends the validated setting to the
144 IEA-15 MW case for a sheared laminar inflow configuration. However, as discussed in the framework
145 of the IEA Wind TCP Task 47 Schepers et al. (2025), turbulent fluctuations appear to have a much
146 stronger impact than shear on load response of aero-elastic numerical codes. Moreover, high-fidelity
147 codes appear rather consistent in predicting loads, while engineering models tend to overpredict fa-
148 tigue loads, particularly for large rotors (Cacciola et al., 2025).

149 The code implements a second-order accurate centered finite difference scheme for the spatial dis-

150 cretization on a staggered Cartesian grid. A hybrid low-storage third-order-accurate Runge–Kutta
 151 (RK) scheme is used for time integration of the non-linear terms (Orlandi, 2012), while the linear
 152 terms are treated implicitly using a Crank-Nicolson scheme. The filtered governing equations are:

$$\frac{\partial u_i}{\partial t} + \frac{\partial u_i u_j}{\partial x_j} = -\frac{\partial p}{\partial x_i} + \frac{1}{Re} \frac{\partial^2 u_i}{\partial x_j \partial x_j} - \frac{\partial \tau_{ij}}{\partial x_j} + \tilde{f}_i, \quad (1)$$

$$\frac{\partial u_i}{\partial x_i} = 0, \quad (2)$$

153 where $i, j \in \{1, 2, 3\}$ represent, in a Cartesian reference frame, the components along the streamwise
 154 (x), wall-normal (y), and spanwise (z) directions, respectively. The Reynolds number $Re = U_\infty D / \nu$
 155 is defined by the undisturbed inlet velocity U_∞ , the turbine diameter D , and the kinematic viscosity of
 156 the fluid ν . These quantities are used as reference values to make the equations non-dimensional. To
 157 solve the filtered equations, a Subgrid-Scale (SGS) stress model is needed. The latter describes the
 158 interaction between the large resolved and the sub-grid unresolved scales, as described by Pino Martín
 159 et al. (2000) and Santoni et al. (2017). Here, we employ the Smagorinsky model with constant
 160 $C_s = 0.09$ as discussed by Martinez-Tossas et al. (2018).

161
 162 The effect of the blades on the flow is modeled by the Actuator Line Model (ALM) (Sorensen
 163 and Shen, 2002), by adding a forcing term to the Navier-Stokes equations, representing the force per
 164 unit volume exerted by the rotor on the fluid. By approximating the rotor blades as straight lines
 165 discretized into segments, it is possible to estimate the lift and drag forces per unit length on a 2D
 166 plane as follows:

$$F_l = \frac{1}{2} \rho u_{rel}^2 C_l(\alpha) c F, \quad F_d = \frac{1}{2} \rho u_{rel}^2 C_d(\alpha) c F, \quad (3)$$

167 where ρ is the air density, c is the local chord, u_{rel} is the relative incoming velocity, α is the angle
 168 of attack, and F represents the tip loss correction factor, which employs the tip-loss model proposed
 169 by Shen et al. (2005). The coefficients c_1 and c_2 of this model have been set in the following way: c_1
 170 has been set to the value reported in the Shen et al. (2005) paper ($c_1 = 0.125$), whereas, c_2 has been
 171 chosen after a calibration with respect to the forces close to the tip reported by OpenFAST for the
 172 same turbine and flow case, leading to the choice of $c_2 = 32$. The forces are then projected on the
 173 flow employing a 2D Gaussian kernel, which spreads the lift and drag force vector, \mathbf{f}^{aero} , in cylinders
 174 surrounding the actuator line,

$$\tilde{\mathbf{f}} = -\mathbf{f}^{aero} \frac{1}{\epsilon^2 \pi} \exp\left[-\left(\frac{r_\eta}{\epsilon}\right)^2\right], \quad (4)$$

175 where r_η is the radial distance of a generic point of the cylinder from the actuator line and ϵ is the
 176 spreading parameter, where $\epsilon/\Delta \geq 2$, with $\Delta = \sqrt{\Delta x^2 + \Delta y^2 + \Delta z^2}$, following Troldborg (2009). The
 177 tower and nacelle are modeled using the Immersed Boundary Method (IBM) following the approach
 178 described by Orlandi and Leonardi (2006).

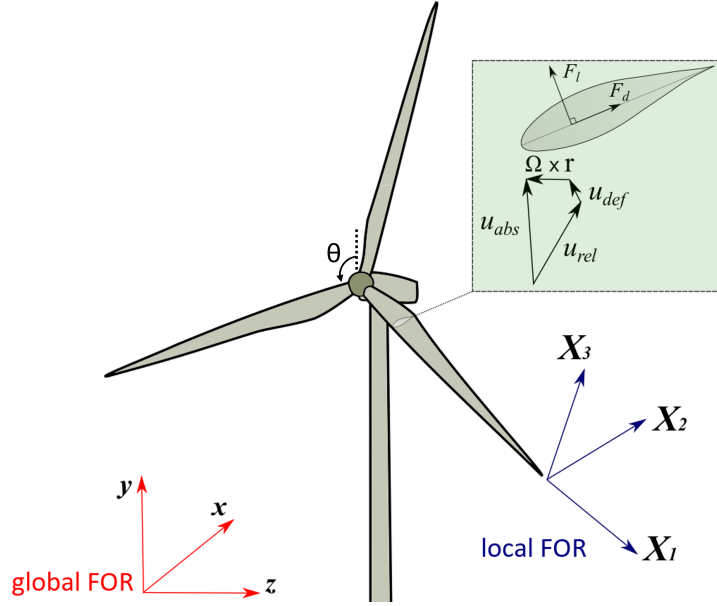


Figure 1: Sketch of the frames of reference used for the CFD and for the CSD simulations.

179 2.1.2 Structural solver

180 From an aerodynamic standpoint, the rotor blades represent the most flexible components within a
 181 wind turbine. Several studies demonstrated that their modal properties have a significant impact on
 182 the dynamics of the entire structure (Damgaard et al., 2013; Dong et al., 2018). Moreover, an analysis
 183 of the isolated blades is also sufficient to accurately estimate the aeroelastic properties of the entire
 184 structure, including the flutter speed (Abdel Hafeez and El-Badawy, 2018). Additionally, the tower
 185 and shaft exhibit minimal deflection due to their stiffness. In light of the above considerations, the
 186 aeroelastic model is constructed to encompass solely the structure of the blades.

187 The structural model used in the present study was extensively described by Della Posta et al. (2022,
 188 2023) and will only be briefly outlined here. Under the assumption of small deformations with respect
 189 to a relative frame of reference (FOR), the blades are assumed to be rotating beams rigidly clamped
 190 at the hub (cantilever beams). Moreover, it is assumed that the blade deformation does not modify
 191 the rotor inertia. With these hypothesis, a linear structural dynamic equation is obtained, taking into
 192 account the Coriolis, centrifugal and Euler effects, that will be given in the following. Let us denote
 193 by X_1 the direction of the pitching axis. This coincides with the neutral axis of the blade, defined
 194 as passing through the quarter of the chord. The direction of the out-of-plane flapwise motion is
 195 indicated by X_2 and is oriented in the positive streamwise direction. The in-plane edgewise direction
 196 of X_3 is defined such that the FOR is oriented as a right-handed coordinate system (Figure 1).

197 Under the assumption of linearity, the elastic generalised displacement $\mathbf{d} = (d_i, \theta_i)$, which includes
 198 translational d_i and rotational θ_i (with $i = \{1, 2, 3\}$) degrees of freedom (DoFs), is decomposed along
 199 the coordinate X_1 on the neutral axis as:

$$\mathbf{d}(X_1, t) = \sum_{m=1}^M q_m(t) \boldsymbol{\psi}^m(X_1), \quad (5)$$

200 where $\boldsymbol{\psi}^m(X_1)$ is the m -th elastic mode shape from the modal analysis of the structure, q_m is
 201 the corresponding modal coordinate, and M is the number of modes used. The effect of the generic
 202 motion of the FOR on the relative structural dynamics (one-way inertial coupling, since we assumed
 203 that the blade deformation does not modify the rotor inertia) is included in a modal basis by means
 204 of the methodology introduced in Reschke (2005) and further developed for the case of wind energy in
 205 Della Posta et al. (2022). Through this method, which exploits the decomposition of the acceleration in
 206 a moving FOR in the virtual work principle, we obtained a system of elastic equations with additional
 207 stiffening, damping, and loading terms depending on the angular velocity and acceleration of the
 208 rotating FOR, as:

$$\mathbf{M}\ddot{\mathbf{q}} + [\mathbf{D} + \mathbf{D}^{Co}(\boldsymbol{\Omega})]\dot{\mathbf{q}} + [\mathbf{K} + \mathbf{K}^c(\boldsymbol{\Omega}) + \mathbf{K}^{Eu}(\dot{\boldsymbol{\Omega}})]\mathbf{q} = \mathbf{e} + \mathbf{e}^c(\boldsymbol{\Omega}) + \mathbf{e}^{Eu}(\dot{\boldsymbol{\Omega}}), \quad (6)$$

209 where \mathbf{M} , \mathbf{D} and \mathbf{K} denote the modal structural mass, damping, and stiffness matrices, respec-
 210 tively, and \mathbf{e} are the external loads expressed in modal basis, including the gravity force acting on
 211 the local centre of mass and the ALM aerodynamic forces acting on the local quarter of chord. The
 212 remaining terms are inherently related to the various contributions to the acceleration in a moving
 213 FOR. Terms with the superscript Co , c and Eu are related to the Coriolis, centrifugal, and Euler
 214 accelerations, respectively. Given the assumption of linearity, we apply all the forces to the reference
 215 undeformed configuration. The discrete evaluation of the additional inertial terms in Equation (6)
 216 is expressed as a function only of the information known from the structural finite-element method
 217 (FEM) model and from the corresponding mode shapes, according to Saltari et al. (2017). For the
 218 modal analysis, performed on the undeformed nonrotating blade, we use a finite element model of
 219 the blade based on complete beam elements with 6 DoFs, with Euler-Bernoulli behavior for bending
 220 in directions X_2 and X_3 , and linear shape functions for axial and torsional deformations. We as-
 221 sume a lumped-mass representation, and we take into account the local offset of the centers of mass
 222 with respect to X_1 . Finally, the structural matrices are assembled considering the local twist. The
 223 generalized- α method (Chung and Hulbert, 1993) is employed to advance the structural dynamic equa-
 224 tion in time, which is unconditionally stable for linear problems, and second-order accurate. Details
 225 about the modal analysis are provided in Appendix A.

226 2.1.3 Fluid-structure interaction model

227 The two-way coupling aeroelastic model employs the ALM sectional approach, whereby the angle
 228 of attack (AoA) and relative velocity are locally modified following the instantaneous blade motion
 229 provided by the structural dynamics. In particular, the distribution of the AoA along each blade
 230 is evaluated as a function of the velocity of the fluid, the angular velocity of the rotor, and the
 231 instantaneous elastic state of the blade (which is projected back to the physical space from the modal
 232 one once the displacement is determined). The latter is generally constructed from the deformation
 233 velocity $\mathbf{u}_{def} = \dot{\mathbf{d}}_{tr}$, considering the time derivative of the translational degrees of freedom only,
 234 and the local vector of the deformation angles $\boldsymbol{\theta}$ (torsion, and in-/out-of-plane angular deformations)

235 derived from the structural solver, which is forced by the updated aerodynamic loads. The algorithm
 236 restricts inter-field communications solely at the beginning of each RK substep, thereby ensuring
 237 optimal computational efficiency. The impact of the torsional dynamics was deemed to be limited
 238 in light of the results obtained in previous studies on the effect of torsion for smaller wind turbines
 239 (Chen, 2017). In order to investigate this issue for the large rotor 15MW wind turbine, in this study we
 240 compare two different CSD models. In particular, we consider as a baseline a two-way coupling that
 241 includes the effect of blade deformation velocity as a sole variable (CFD-CSD/OV, for Only Velocity),
 242 and a more complete model including the torsional deformation in the coupling (CFD-CSD/T, for
 243 Torsional). In general, the relative velocity for a rotating blade can be defined with the following
 244 expression:

$$\mathbf{u}_{rel} = \mathbf{u}_{abs} - \boldsymbol{\Omega} \times \mathbf{r}_{OP} - \mathbf{u}_{def}, \quad (7)$$

245 where \mathbf{u}_{abs} is the filtered velocity from the fluid solver at the actuator line, \mathbf{r}_{OP} is the general radial
 246 vector pointing to the considered section, $\boldsymbol{\Omega}$ is the rotor rotational speed, and \mathbf{u}_{def} is the deformation
 247 velocity of the structure at the same position. As a result, the AoA used to determine the air load
 248 coefficients is defined as follows:

$$\alpha = \text{atan} \left(\frac{\mathbf{u}_{rel} \cdot \mathbf{E}_2}{-\mathbf{u}_{rel} \cdot \mathbf{E}_3} \right) - \phi - \theta_{tors} = \text{atan} \left[\frac{(\mathbf{u}_{abs} - \mathbf{u}_{def}) \cdot \mathbf{E}_2}{\Omega r - (\mathbf{u}_{abs} - \mathbf{u}_{def}) \cdot \mathbf{E}_3} \right] - \phi - \theta_{tors}, \quad (8)$$

249 where ϕ is the local twist angle of the blade, θ_{tors} is the local torsional deformation, \mathbf{E}_i are the
 250 unit vectors of the relative FOR rotating with the structure, and hence, $v_2 = \mathbf{u}_{def} \cdot \mathbf{E}_2$ is the flapwise
 251 deformation velocity component, and $v_3 = \mathbf{u}_{def} \cdot \mathbf{E}_3$ is the edgewise deformation velocity component.
 252 The simplified coupling procedure benefits from the sectional one-dimensional formulation of the
 253 ALM, which avoids the complex treatment of the fluid-solid interface with the associated kinematic
 254 and traction conditions.

255 3 Flow and structural setup

256 In this work, we consider a stand-alone IEA 15-MW wind turbine (Gaertner et al., 2020b) in its
 257 monopile configuration. This wind turbine has a rotor diameter $D = 240$ m with three blades of
 258 length $L = 117$ m. Table 1 provides the main features of the turbine.

259 The computational domain has dimensions $12.5 \times 5 \times 3$ diameter units, as shown in Figure 2. The
 260 distance of the turbine from the inlet of the computational domain (equal to 4D) has been determined
 261 on the base of the reference data available in the literature, which vary in the range 2D-5D. Smaller
 262 distances from the inlet (2D) have been employed for experimental set-up (Bartl and Satran, 2017;
 263 Krogstad et al., 2015), whereas larger distances (in the range 2.7D-5D) are typical of numerical
 264 simulations (Porte-Agel and Wu, 2011; Ciri et al., 2017; Allah and Sha ei Mayam, 2017; Stevens et al.,
 265 2018). Moreover, we have verified numerically that pressure fluctuations do not generate spurious
 266 reflections at the inlet section in our simulations. The spanwise length of the computational domain
 267 (equal to 3D) is the same employed in previous numerical simulations (Ciri et al., 2017; Allah and
 268 Sha ei Mayam, 2017). We have verified that, using periodic boundary conditions, the blockage effect

269 on the single turbine is negligible. Moreover, following the convergence study reported in the Appendix
 270 A, the computational box has been discretized by a staggered grid composed of $2049 \times 513 \times 513$ points
 271 in the streamwise, wall-normal, and spanwise directions, respectively. The orthogonal grid is equally
 272 spaced in the streamwise and spanwise directions and is stretched vertically, with a gradually wider
 273 spacing starting from the region above the rotor. The grid spacing described leads to an actuator line
 274 discretized by 86 points per blade. The time resolution of the LES computation is tied to the spatial
 275 resolution, as defined by the stability requirements of the numerical scheme adopted. Simulations are
 276 carried out at a constant Courant–Friedrichs–Lewy (CFL) number (Courant et al., 1967) $CFL = 0.65$,
 277 which ensures an average time step $\overline{\Delta t} = 0.024s$. The turbine location is 4 diameter units from the
 278 inlet and centered in the spanwise direction. Furthermore, we impose a sheared laminar inflow velocity
 279 profile, defined by a power law with the exponent $\alpha = 0.05$, and a convective outlet boundary condition,
 280 i.e., $\frac{\partial u_i}{\partial t} + C \frac{\partial u_i}{\partial x} = 0$, with the constant C set to the average value of the outflow velocity. Notice that,
 281 as the shear is imposed at the inlet, the flow profile is allowed to change when reaching the turbine.
 282 However, since the power law profile complies with the no-slip conditions at the wall and with the slip
 283 conditions at the free-stream, the modifications are mostly due to the slight three-dimensionalization
 284 of the flow due to the presence of the turbine. In the spanwise direction, periodic boundary conditions
 285 are imposed. Moreover, slip and no-slip conditions are enforced at the top and bottom boundaries,
 286 respectively. The turbine is subjected to a flow with a Reynolds number $Re \approx 10^8$ and operates at
 287 its nominal tip speed ratio (TSR) of $\lambda = 9$. The streamwise undisturbed velocity at the hub height
 288 is constant and equal to $U_\infty = 10 \text{ m/s}$. The simulations were conducted for a time interval of 300 s
 289 over the initial transient, which corresponds to 35 revolutions of the rotor.

290 To identify the optimal configuration for the structural model, we conducted a preliminary sensitivity
 291 analysis and then validated the structural eigenfrequencies of the undeformed nonrotating blade with
 292 the results found in the literature. A more detailed insight into this analysis is presented in Appendix
 293 B, where the structural properties of this turbine are shown. Finally, a number of modes $M_s = 15$
 294 and a structural discretization of the blades given by $N = 80$ equally-spaced nodes were chosen.
 295 For comparison purposes, wind turbine simulations have been also conducted using the OpenFAST
 296 solver *Release v3.2.0* (July 29, 2022). The aerodynamic computations are performed by the *AeroDyn*
 297 (Jonkman et al., 2015) module which is based on the BEM theory. A Prandtl loss model is applied
 298 to account for the tip and root effects. The structural module dedicated to the computation of the
 299 blade deformation is contained in the *BeamDyn* module, which relies on the geometrically exact beam
 300 theory and may resolve geometric non-linearities and large deflections (Wang et al., 2016b). In order to
 301 compare the CFD-CSD results with a modal structural analysis, we also performed simulations using
 302 the standalone *ElastoDyn* module, based on a modal approach and suitable for blade deformation
 303 dominated by bending. It is worth to notice that the latter does not take into account the torsional
 304 degree of freedom, so it is to be directly compared to the CFD-CSD/OV model, which also does not
 305 account for the coupling between the torsional deformation and the angle of attack. As reported in the
 306 original manual of *AeroDyn* (Moriarty and Hansen, 2005), OpenFAST couples the fluid and structural
 307 solvers in a similar way to our CFD-CSD solvers. In particular, the local angle of attack is determined
 308 taking into account the local deformation velocities.

Parameter	Units	Value
Power rating	MW	15
Rotor diameter (D)	m	240
Rotor orientation	–	Upwind
Number of blades	–	3
Blade length (L)	m	117
Hub height	m	150
Hub radius (R_{hub})	m	3.97
Rated wind speed	m/s	10.59
Design tip speed ratio	–	9
Maximum rotor speed	RPM	7.56

Table 1: IEA 15-MW (Gaertner et al., 2020b) wind turbine main features

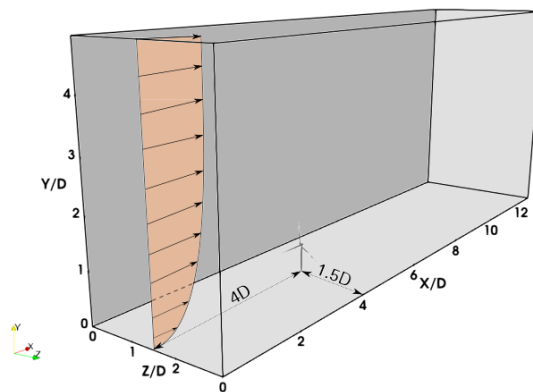


Figure 2: Sketch of the computational domain where the incoming sheared flow and the position of the turbine are highlighted.

309 4 Results and discussion

310 This section presents the results of two set of simulations: one modeling a rotor-only configuration
311 (RO) and the other including the tower and nacelle (TN). Furthermore, both configurations are sub-
312 jected to comparative analysis using the OpenFAST submodules. Firstly, the near-wake aerodynamic
313 characteristics and the wake recovery of both configurations determined by the CFD-CSD solvers are
314 discussed. Then, the aerodynamic loads on the blades are analyzed and the outcomes from both solvers
315 are compared. Finally, the overall turbine performance and the effects on the blade deformation are
316 assessed.

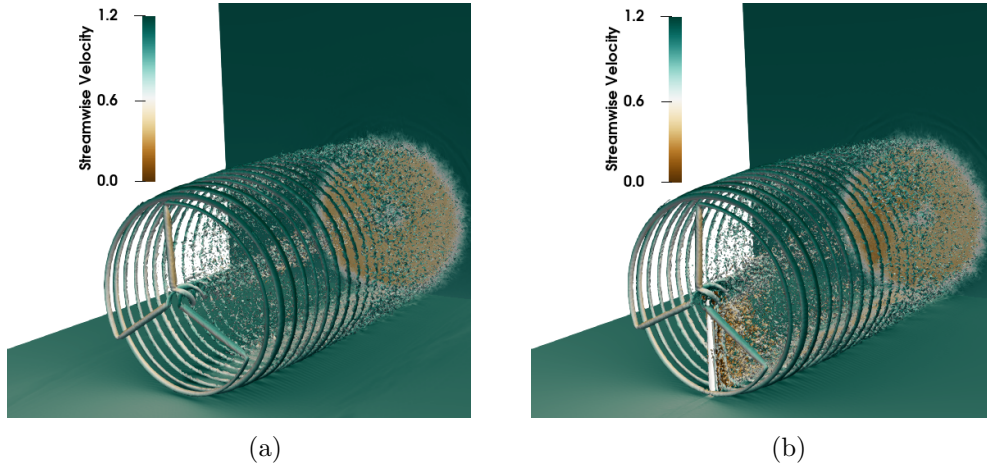


Figure 3: Q-criterion contour of the instantaneous velocity field colored by the streamwise velocity for the rotor-only case (RO) (a) and tower and nacelle (TN) (b).

317 4.1 Flow analysis

318 As a first step, we analyze the flow field variables, as obtained using the CFD-CSD/T solver. Figure
 319 3 illustrates the main coherent flow structures in the field by means of an instantaneous isosurface
 320 of the Q-criterion colored by the streamwise velocity for both cases. It is evident that the presence
 321 of the tower affects the vorticity intensity distribution along the vertical direction. In particular, the
 322 occurrence of a low-velocity recirculation zone at the tower height for the TN case can be identified,
 323 which is a result of the tower shadowing (see Figure 3b). Moreover, the TN case demonstrates a more
 324 rapid dissolution of the endogenous coherent hub vortex structures if compared to the RO case (see
 325 Figure 3a). On the other hand, the tip vortex structures appear to be minimally influenced by the
 326 presence of the tower. Figure 4 shows the rotor-averaged streamwise velocity along the flow direction,
 327 time-averaged over 30 revolutions of the rotor. Contrary to what Santoni et al. (2017) observed in
 328 their work on the 5MW reference turbine invested by a uniform inflow (see the red lines in figure 4),
 329 the rotor-averaged velocity for the TN configuration in the wake remains slightly lower than for the
 330 RO case, indicating that wake recovery is slightly hindered by the presence of the tower. In order to
 331 establish whether this opposed behaviour with respect to the results of Santoni et al. (2017) may be due
 332 to the different inflow or rather on geometrical features characterizing the two different turbines, we
 333 have carried out a computation equivalent to that of the 15MW turbine (sheared inflow, $U_\infty = 10m/s$
 334 etc.), but for an NREL 5MW wind turbine. As shown by the blue lines in figure 4, as in Santoni et al.
 335 (2017), the rotor-averaged velocity for the TN configuration in the wake remains rather higher than
 336 for the OR case, indicating that wake recovery for an NREL 5MW turbine is indeed advanced by the
 337 presence of the tower, no matter the inflow considered. Whereas, the larger gap between the RO/TN
 338 cases observed in the near wake by Santoni et al. (2017) is not observed in this case, and it is thus
 339 probably due to the uniform inflow. Comparing these results to the present data, we can conclude
 340 that the slower wake recovery observed for the 15MW turbine in the presence of the tower appears
 341 to be due to geometrical features of the turbine itself, not to the inflow characteristics. One possible

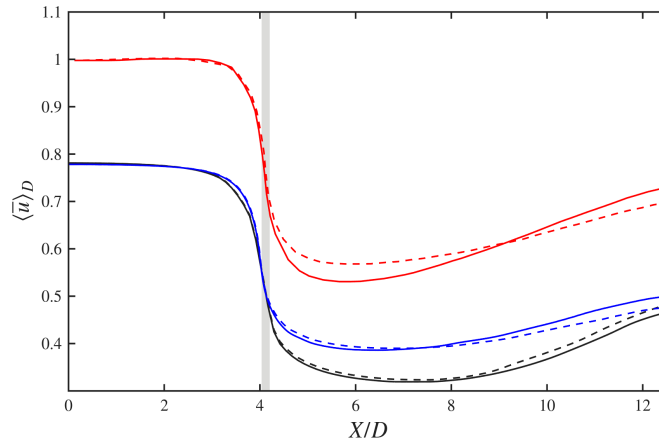


Figure 4: Rotor-averaged velocity along the streamwise direction normalized by the undisturbed velocity at the rotor height, namely, $U_\infty = 10 \text{ m/s}$, for the present data (black curves), a computation of the NREL 5MW turbine for the same configuration and inflow (blue curves) and the work of Santoni et al. (2017) (red curves). The grey region represents the area covered by the rotor. (RO - - -, TN —).

342 explanation for this behaviour could be differences in the tower-to-rotor aspect ratio. In particular,
 343 for the NREL 5-MW turbine, the ratio between the tower diameter and the rotor diameter is about
 344 equal to 0.047, whereas, for the 15MW turbine, it is only about 0.027 (the tower diameters being 6m
 345 and 6.5m, respectively). Thus, the thinner shape (in terms of diameter units) of the tower, as well as
 346 the lower value of the incoming velocity at the tower height due to the presence of shear at the inflow,
 347 result into a decreased mixing behind the turbine which leads to a slower wake recovery.

348 Although not favoring wake recovery, the tower still plays a strong role in the wake dynamics, as it
 349 can be visualized in Figure 5, showing slices of instantaneous streamwise velocity at different tower
 350 heights corresponding to 80% of the blade (top) and to the tip of the blade (bottom), when the blade
 351 is in front of the tower, i.e. $\theta = 180^\circ$ (left), and when it is far from it (right). In particular, it can
 352 be observed that the turbulent mixing right downstream of the tower is already very high in the near
 353 wake compared to that close to the tip of the blades. Due to the mutual effect of the asymmetry
 354 induced by the rotation of the blades and of the wake meandering, it can be seen that, inside the
 355 rotor disk, the tower wake bends in the spanwise direction (Figure 5, top frames), whereas it is rather
 356 spanwise independent at a height corresponding to the blade's tip (bottom frames). Moreover, one
 357 can see that the passage of the blade in front of the tower (left frames) induces a strong perturbation
 358 in the flow field already upstream of the tower. In the following section, the effect of this perturbation
 359 on the phase oscillations of several relevant quantities (aerodynamic forces, power coefficient, etc.)
 360 will be discussed.

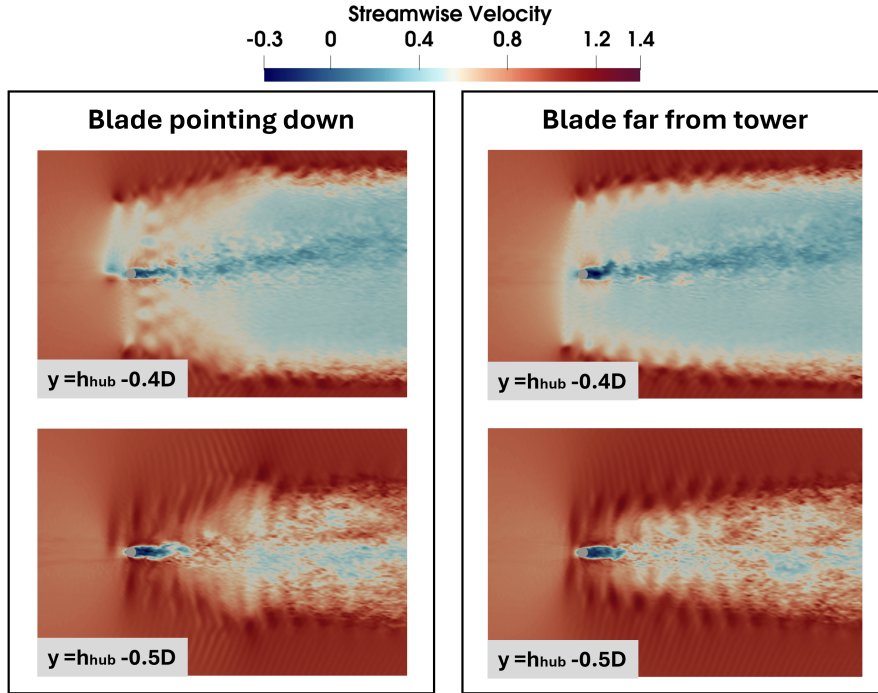


Figure 5: Instantaneous streamwise velocity on horizontal slices at different tower heights corresponding to 80% of the blade (top slices), and the tip of the blade (bottom slices). In the left configuration, the blade is in front of the tower ($\theta = 180^\circ$), while on the right the blade is far from the tower. $h_{hub} = 0.625D$ is the hub height.

4.2 Aerodynamic loads on the blade

The analysis of the aerodynamic loads on the blade has been conducted using the present CFD-CSD models and the engineering software OpenFAST. The same laminar sheared inflow is imposed for both solvers using a power law with the same exponent and reference streamwise velocity at the hub height. We have chosen not to impose a turbulent inflow to avoid differences in the definition of the turbulent inflow itself which might have hindered the comparison between the results of the two codes. It is important to note that the four solvers employed differ in both their aerodynamic and structural modeling approaches. Moreover, the flow that impacts the turbine is not exactly the same for the CFD and OpenFAST solvers, since in the former case it is imposed at several diameters upstream the rotor plane. As a result, it is not always possible to unambiguously determine whether the observed discrepancies in the results originate from the fluid-dynamic models or from the structural formulations.

Figure 6 depicts the following time-averaged aerodynamic quantities along the span of the blade: the local angle of attack α (Figure 6a); the aerodynamic pitching moment per unit length M_{aero} (Figure 6b); the flapwise and edgewise components (normal and tangential to the rotor disk, respectively) of the aerodynamic force per unit length F_2 (Figure 6c) and F_3 (Figure 6d), respectively. In particular,

377 Figure 6a shows that a good agreement of the local incidence angle computed by both CFD-CSD mod-
 378 els (solid lines) with that computed by *ElastoDyn* (circles) and *BeamDyn* (squares) is obtained from
 379 the 20% up to the 80% of the blade length. Indeed, the differences in the root area could be ascribed to
 380 the presence of the hub which is modeled differently by the solvers. The discrepancy of the incidence
 381 angle observed towards the tip subsequently affects the aerodynamic loads. The F_2 force in Figure 6c
 382 shows a very good fit of the CFD-CSD/T results with that of the nonlinear solver *BeamDyn*, despite
 383 the linearity of our in-house CSD model. The strong discrepancies with respect to the values obtained
 384 by *ElastoDyn* can be ascribed to the absence of the torsional deformation in the latter solver. Indeed,
 385 the CFD-CSD/OV solver, which neglects the torsional feedback in the coupling, shows very similar
 386 results to the *ElastoDyn* solver. A similar effect can be observed by examining the reduction in F_3
 387 towards the tip of the blade (see Figure 6d). The distribution of the aerodynamic pitching moment
 presents instead a maximum gap of about 8% from the BEM-based solvers.

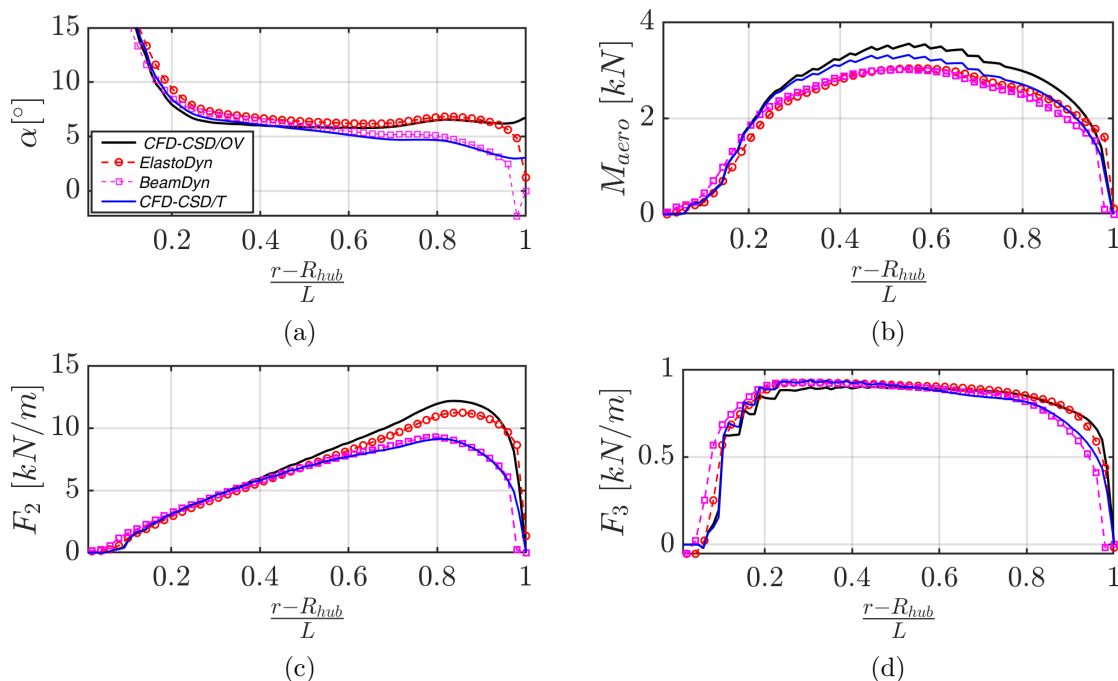


Figure 6: Average aerodynamic quantities along the blade compared between CFD-CSD/OV, CFD-CSD/T, *ElastoDyn*, and *BeamDyn*. (a) Incidence angle, (b) Aerodynamic pitch moment, (c) flapwise aerodynamic force, (d) edgewise aerodynamic force.

388 As demonstrated by Hansen (2015), the outer third of the blade span is the most critical region in
 389 terms of deflections and deformations due to the combination of higher aerodynamic loads and reduced
 390 structural stiffness. Therefore, a phase average of the aerodynamic quantities at the 80% of the blade
 391 has been performed. Figure 7 reports the evolution of the incidence angle and of the aerodynamic
 392 force components at $\frac{r-R_{hub}}{L} = 0.8$ (being R_{hub} the hub radius and L the blade length) versus the blade
 393 rotation angle θ . The dynamical behavior of the aerodynamic quantities in the presence (solid lines) or
 394

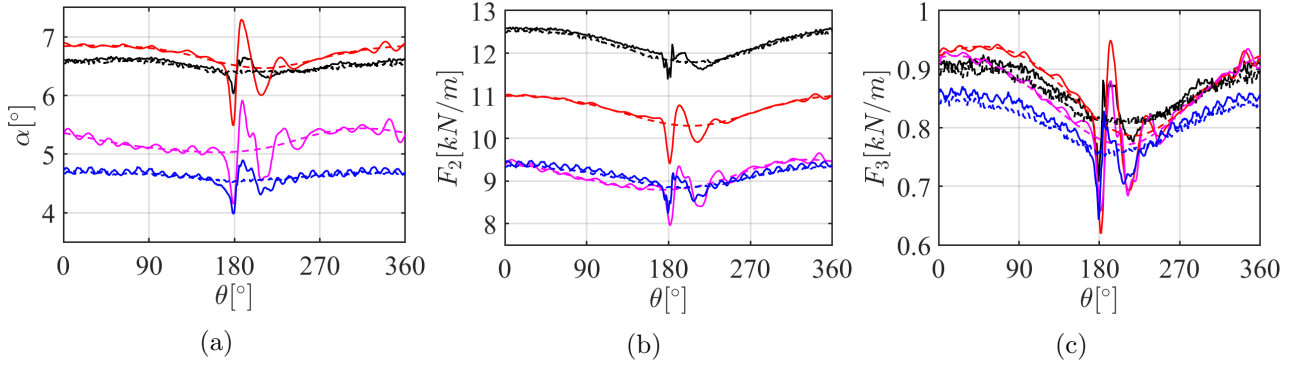


Figure 7: Phase-averaged values of: (a) the local incidence angle, (b) flapwise aerodynamic force, and (c) edgewise aerodynamic force at the 80% of the blade. CFD-CSD/OV: TN —, RO ----. CFD-CSD/T: TN —, RO ----. *ElastoDyn*: TN —, RO ----. *BeamDyn*: TN —, RO ----.

395 in the absence (dashed lines) of the tower underlines that the passage of the blade in front of the tower
 396 represents the main source of instability for the flow conditions considered. Indeed, the blade-tower
 397 interaction leads to oscillations of the aerodynamic forces and of the incidence angle around $\theta = 180^\circ$,
 398 i.e., when the blade is pointing down. However, unlike the case of the NREL 5-MW turbine (Bernardi
 399 et al., 2023), this effect appears to be stronger for the BEM computations than for the CFD-CSD
 400 solver. Concerning this point, we should recall that, as pointed out by Bernardi et al. (2023), the
 401 complex flow dynamics resulting from the interaction between the blade and the tower, shown in
 402 Figure 5, may not be well described by OpenFAST, which uses a simple potential flow model. It can
 403 be observed that, between the rotor and the tower, a region with low streamwise velocity is observed.
 404 We can expect that the passage of the blade in front of the tower thus induces an alteration of the
 405 aerodynamic forces on the blade due to the decrease/increase of the streamwise velocity. This issue
 406 will be further discussed in the following, where a possible reason for the different behavior observed
 407 for the IEA 15-MW with respect to the NREL 5-MW turbine will be discussed.

408 Apart from the effect of the tower, one can observe a rather good match between the CFD-CSD/OV
 409 and *ElastoDyn* solvers for both the incidence angle and the edgewise component of the aerodynamic
 410 force, while the flapwise component presents some discrepancies. On the other hand, when torsional
 411 feedback is included, CFD-CSD/T and *BeamDyn* solvers, regardless of the linearity or non-linearity of
 412 the models, agree rather well on the aerodynamic forces, especially on the flapwise one, which shows
 413 an error $\approx 2\%$, while the edgewise force reaches a $\approx 5\%$ error at azimuthal angles close to $\theta = 0$.
 414 Whereas, the error between the two solvers on the angle of attack reaches 8% .

415 To better investigate the local response of the different models during the blade revolution, we con-
 416 ducted a comparative analysis of the aerodynamic loads, employing phase-averaged quantities over
 417 the span. Figure 8 illustrates the percentage difference of the phase-averaged aerodynamic quantities
 418 on the rotor plane of the *ElastoDyn* (*BeamDyn*) solver with respect to the CFD-CSD/OV, defined as
 419 $|\langle \Delta\alpha/\alpha^{CFD-CSD/OV} \rangle\%|$, and of the CFD-CSD/T model, defined as $|\langle \Delta\alpha/\alpha^{CFD-CSD/T} \rangle\%|$, respec-
 420 tively. In particular, in comparison to *ElastoDyn*, a higher value of the absolute incidence angle in the
 421 range of $|\langle \Delta\alpha/\alpha^{CFD-CSD/OV} \rangle\%| = [17\%, 25\%]$ is found in the zone after the tower (see Figure 8a).

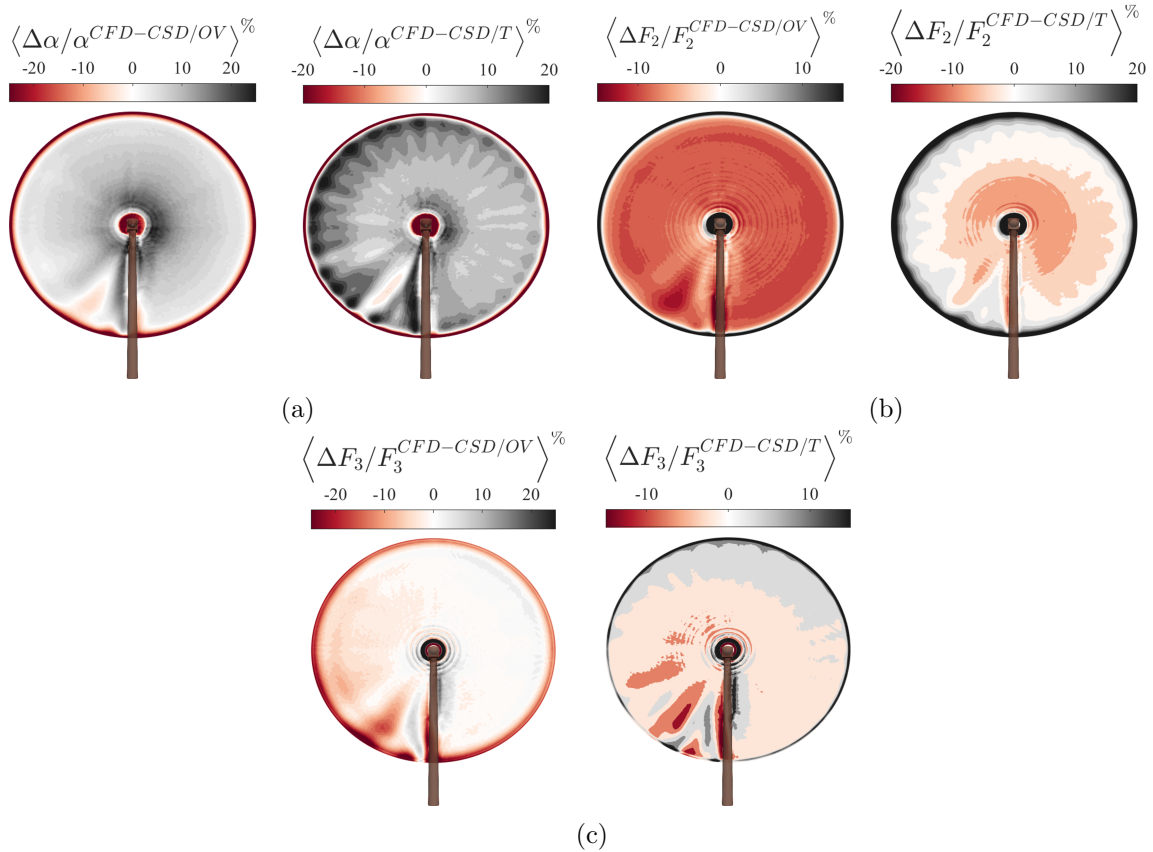


Figure 8: Phase-averaged contour plots of the percentual differences of the aerodynamic quantities between CFD-CSD/OV versus *ElastoDyn* (left), and CFD-CSD/T versus *BeamDyn* (right), respectively. (a) Incidence angle, (b) flapwise aerodynamic force, (c) edgewise aerodynamic force.

422 The difference with respect to the results obtained by *BeamDyn* tends to be higher moving from the
423 root to the tip with a discontinuity in the tower area, spanning the range $|\langle \Delta\alpha/\alpha^{CFD} \rangle\%| = [35\%, 60\%]$
424 in the last 20% of the blade span. Furthermore, the angle of attack distribution affects the components
425 of the aerodynamic force. In fact, the distribution of the flapwise component of the force follows the
426 same pattern of the incidence angle (see Figure 8b). On the other hand, for the edgewise component
427 the major discrepancies are concentrated in the final radial sections of the blade toward the tip (see
428 Figure 8c). In general, we can conclude that the most significant discrepancies are observed in the
429 tip region where the three-dimensional effects are more relevant and where the complexity of the fluid
430 flow is strongly affected by the presence of the tower.

431 Notably, similar discrepancies are observed when comparing the CFD-CSD/T solver with the *Beam-*
432 *Dyn* solvers. However, in this case some high-frequency oscillations are observed for the three aerody-
433 namic quantities. In fact, the same oscillations are observed in the phase averaged quantities at 80%
434 of the blade shown in Figure 8, for both the CFD-CSD/T solver and *BeamDyn*. The frequency of
435 these oscillations computed by the two solvers appear very close and comparable with the natural fre-

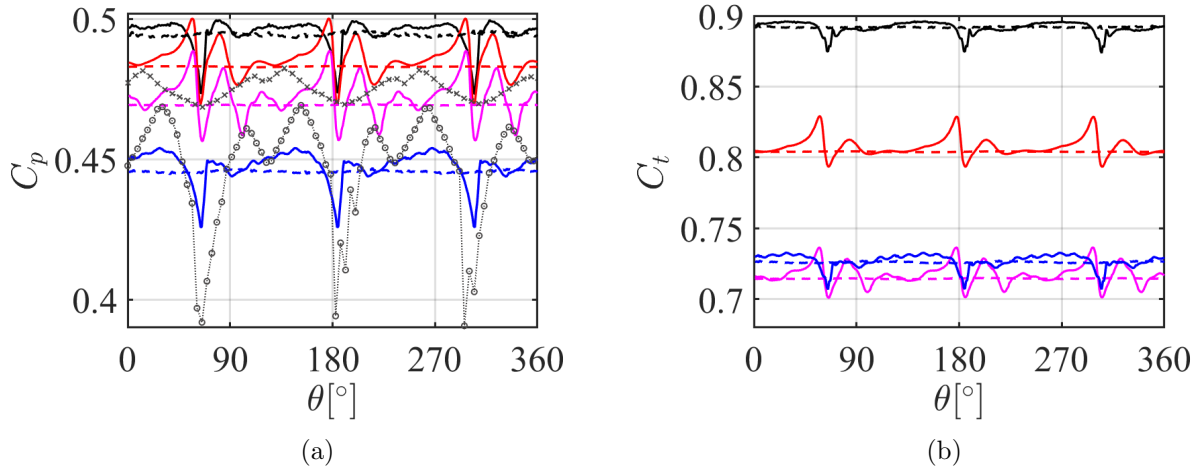


Figure 9: Phase-averaged power (a) and thrust (b) coefficients. CFD-CSD/OV: TN —, RO ----. CFD-CSD/T: TN —, RO ----. *ElastoDyn*: TN —, RO ----. *BeamDyn*: TN —, RO ----. From figure 3 of Bernardi et al. (2023): \circ *LES + CSD flexible*, \times *OpenFAST-AeroDyn*.

436 quency of the first torsional mode, although some differences can be observed in the amplitudes of the
 437 signals, especially concerning the angle of attack ($\approx 8\%$ of error) and the edgewise aerodynamic force
 438 at azimuthal angles close to zero ($\approx 6\%$ of error). Again, this observation indicates that including the
 439 torsional degree of freedom in the structural solver is crucial for describing accurately the amplitude
 440 and dynamical behaviour of the aerodynamic quantities.

441 4.3 Power and thrust coefficients

442 The aerodynamic loads previously presented are also useful to evaluate the power and thrust coeffi-
 443 cients, defined as follows:

$$C_p = \frac{P_d}{\frac{1}{2}\rho AU_\infty^3}, \quad C_t = \frac{T_{aero}}{\frac{1}{2}\rho AU_\infty^2}, \quad (9)$$

444 where $A = \pi D^2/4$ represents the rotor area, P_d is the aerodynamic power transferred to the rotor and
 445 T_{aero} is the overall aerodynamic thrust on the turbine.

446 Starting from the time history of C_p and C_t , we computed their phase-averaged evolution as reported
 447 in Figure 9. The periodic passage of the blades in front of the tower for the TN configuration produces
 448 a drop of the curves of about 10%. Eventually, the performance is restored to the value obtained in the
 449 RO case following the elastic dynamical behavior of the structure. The results reflect the dependency of
 450 the power and thrust coefficients on the edgewise aerodynamic force F_3 and the flapwise aerodynamic
 451 force F_2 at the 80% of the blade, respectively (see Figures 7c and 7b), which are strongly influenced
 452 by the presence of the tower. Notice that, also here, we can observe that the drop in the C_p curve
 453 appears to be rather similarly predicted by BEM and CFD, although the BEM prediction exhibits
 454 notable oscillations before and after the drop, whereas these are not present in the CFD results. A
 455 different behaviour was observed for the NREL 5-MW turbine (as in figure 3 of Bernardi et al. (2023),

456 included in Figure 9 of the present paper with symbols), where this performance drop is considerably
 457 underestimated by the BEM computations. A possible factor that may contribute to this different
 458 behaviour may reside in the different relative geometry of the two wind turbines. Indeed, the flow
 459 induced by a thinner tower (in diameter units), as in the case of the 15-MW wind turbine, might be
 460 better described by a potential flow solution compared to the one induced by a thicker tower, as in
 461 the case of the 5-MW wind turbine, and may thus lead to the observed improved agreement between
 462 BEM and CFD results. Moreover, the differences in the flow impinging on the blade might also have
 463 an effect. In fact, in Bernardi et al. (2023) a uniform inflow was imposed. Whereas, in the present
 464 case, due to the shear imposed at the inflow and the limited distance from the ground of the tip of the
 465 blade (only $\approx 0.125D$ for the 15MW turbine), the blade is invested by a flow having a much smaller
 466 velocity compared to the given value of U_∞ at hub height, further confirming the increased suitability
 467 of a potential flow solution upstream of the tower. Nevertheless, we should recall that this remains a
 468 very strong approximation, as also demonstrated by the differences in the forces and angles that have
 469 been observed in the previous section (see Figure 8, for instance).

470 It can be concluded that the performance loss induced by the passage in front of the tower is less
 471 pronounced for the 15 MW NREL turbine in the present configuration ($\approx 5\%$) compared to the 5
 472 MW turbine in the configuration considered in Bernardi et al. (2023) ($\approx 15\%$, see figure 3 of this
 473 reference), with both BEM theory and CFD yielding similar predictions in the case of the 15 MW
 474 turbine. However, it is worth recalling again that Bernardi et al. (2023) considered a uniform inflow,
 475 whereas here the inflow is sheared. This can be a possible reason for this different behaviour, since
 476 the lower wind speed in the lower part of the rotor plane leads to a lower production in the bottom
 477 half of the rotor plane, where the tower is located. This may cause a smaller performance drop due
 478 to the tower relative to the total produced power. Therefore, the observed difference can be not only
 479 due to the change in turbine size, but also due to the change in inflow conditions.

480 Moreover, the present results predict that, for very large rotors and a sheared inflow, the tower effect
 481 on blade deformations is less pronounced than for smaller rotors, although it should yet be taken into
 482 account for accurately describing the turbine’s performance oscillations as it still represents a major
 483 source of unsteadiness.

484 The average value of the power coefficient is much larger when the torsional deformation is neglected.
 485 This feature is observed by both CFD and BEM approaches. However, one can observe that *ElastoDyn*
 486 underestimates the value of C_p with respect to the corresponding non-torsional CFD model, while the
 487 opposite is observed when comparing *BeamDyn* with the torsional CFD solver. This is probably due
 488 to the fact that *BeamDyn* predicts higher values of the aerodynamic edgewise forces with respect to
 489 the CFD-CSD/T approach, which are linked to a smaller torsional deformation as will be shown in
 490 figure 11f in the next section.

491 Figure 10 shows the premultiplied Power Spectral Density (PSD) of the power (Figure 10a) and thrust
 492 (Figure 10b) coefficients evolution. The PSD is normalized by the variance of each coefficient σ^2 and
 493 plotted versus the frequency normalized by the rotational frequency of the rotor, f/f_{rot} where the
 494 latter is denoted as $1P = f_{rot} = 7.5RPM$ and its multiples will be denoted as $2P, 3P$ etc. In both
 495 cases, the CFD-CSD solvers seem to provide a richer representation of the aerodynamic coefficients,
 496 capturing the full range of flow-structure interactions. Indeed, an examination of the low-frequency
 497 behavior reveals that both quantities exhibit isolated low-frequency peaks when using the BEM-based

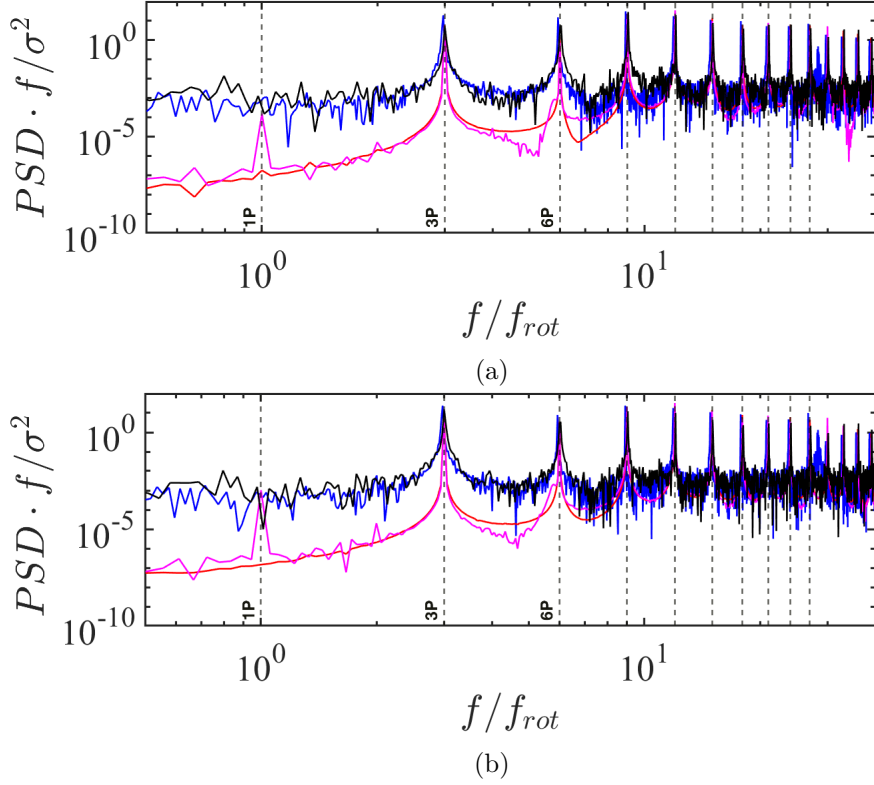


Figure 10: Power Spectral Density (PSD) of the power (a) and thrust (b) coefficients. The vertical dashed lines highlight the rotational frequency of the rotor $1P = f_{rot} = 7.5RPM$ and the multiples of $3P$, respectively. CFD-CSD/OV —, CFD-CSD/T —, *ElastoDyn* —, *BeamDyn* —.

498 solvers, a phenomenon not observed with the CFD-CSD, where the low-frequency range is rather
 499 broadband and does not present particular peaks. It is important to notice that the frequency 1P can
 500 be directly linked to the frequency of the passage of the blade in front of the tower, but also to wind
 501 shear loads on the blades. Concerning the first point, a potential flow solution as that used in the
 502 BEM solver is keen to provide a simple, single-frequency response, whereas a complex, turbulent flow
 503 is expected to result in a more broadband spectrum. Concerning the second point, we have to consider
 504 that in LES, the power law profile is imposed at the inlet of the domain but it is free to evolve for
 505 4 diameters before the wind turbine, altering in a non-trivial way the flow field and the consequent
 506 frequency response of the blades. This outcome indicates that the BEM-based solvers tend to overcut
 507 the power oscillations associated with low-frequencies that are not exactly equal to 1P or 2P. For all
 508 solvers, however, the strongest PSD peaks are to be found at much larger frequencies (3P-6P-9P-12P),
 509 as also observed by Pagamonci et al. (2023) by means of URANS aeroelastic simulations of the NREL
 510 5-MW, the DTU 10-MW, and the IEA 15-MW turbines. One can also notice that the amplitude
 511 associated with the 3P frequency appears to be consistently described by the two solvers, although
 512 also in this range the BEM solver appears to overdamp the frequencies in between different peaks.
 513 Moreover, a good agreement is evident between the two set of results concerning the value of the

514 frequencies and the level of the PSD for frequencies that are multiples of $3P$.

515 4.4 Structural response

516 This section presents the analysis of the structural dynamics. Figure 11 reports the phase-averaged
517 dynamic response of the free extremity of the blade (left column) and the time-averaged deforma-
518 tion of the entire span (right column). Figure 11a shows how the out-of-plane deformation is mainly
519 governed by the aerodynamic component of the force normal to the rotor plane and, hence, to the
520 aerodynamic effects, heavily affected by the tower. In fact, it is visible how the tower placed at
521 $\theta = 180^\circ$ produces a drop in the deformation, followed by an elastic dynamic response which restores
522 the value far from the pointing-down position. The time-averaged maximum deformation predicted
523 by the CFD-CSD/OV solver is 16% higher compared to the *ElastoDyn* module and 17% compared
524 to *BeamDyn* (see Figure 11b). On the other hand, the same quantity predicted by the CFD-CSD/T
525 solver is 17% lower compared to the *ElastoDyn* module and 13% compared to *BeamDyn* (see Figure
526 11b). This is consistent with the fact that including the torsional degree of freedom reduces the loads
527 (see figure 7b) and the resulting deformation. Although the trend of deformation with respect to the
528 blade span appears similar to previous predictions based on URANS (see Pagamonci et al. (2023)),
529 the out-of-plane deformation is rather larger, reaching 16 m at the blade’s tip. The amplitude of the
530 deformation is however close to that obtained by Trigaux et al. (2024) using LES. Figure 11c depicts
531 instead the in-plane deformation, which is mostly due to gravity. The results show that the shadowing
532 effect of the tower does not influence this quantity, which is expected as the lag deformation is mainly
533 driven by gravity. Furthermore, the discrepancies obtained between *ElastoDyn* and *BeamDyn* can be
534 attributed to the lack of modes used by the former model to describe the translation in the edgewise
535 direction (see Figure 11d). The discrepancy does not seem to be linked to the linearity of this model,
536 as the result of the CFD-CSD/T solver, which is linear as well, is much closer to the *BeamDyn* results.
537 Moreover, the results of the CFD-CSD/OV and the CFD-CSD/T models are very close each other.
538 It can be noticed that the amplitude of the oscillation of the in-plane deflection is consistent with
539 that reported by Trigaux et al. (2024) (see Figure 7b of their paper, reporting an oscillation between
540 ≈ -2.3 and ≈ 0.2), although the sign is opposite due to the different frame of reference used.
541 A further significant insight into the deformation phenomenon is provided by the torsional DoF. Figure
542 11e shows a comparison of the torsional angle at the tip with *BeamDyn*. Significant discrepancies can
543 be observed between the LES and the BEM approaches, which cannot be reconducted to the different
544 coupling procedures adopted by the models. On the one hand, *BeamDyn* and CFD-CSD/T both take
545 into account the deformation angle in the coupling (Wang et al., 2016b), while in the CFD-CSD/OV
546 solver the angle of attack depends only on the deformation velocity (see Equation 8). However, the
547 gap between the BEM and the CFD-CSD/T curves is quite large, reaching approximatively 20%
548 of the torsional deformation value. These differences likely arise from the combined effects of both
549 aerodynamic and structural modeling approaches used in BEM and LES. Although in the present
550 paper we have mostly focused on a comparison of the structural models, a thorough comparison of
551 the aerodynamics modeling can be found in the report of IEA Task 47 Schepers et al. (2025), where
552 results produced with the present code are included (see, for instance, figure 4.25 and following for
553 non flexible blades). The discrepancy between the BEM and the CFD-CSD results is confirmed by
554 the time-averaged torsional deformation along the span reported in Figure 11f where the maximum

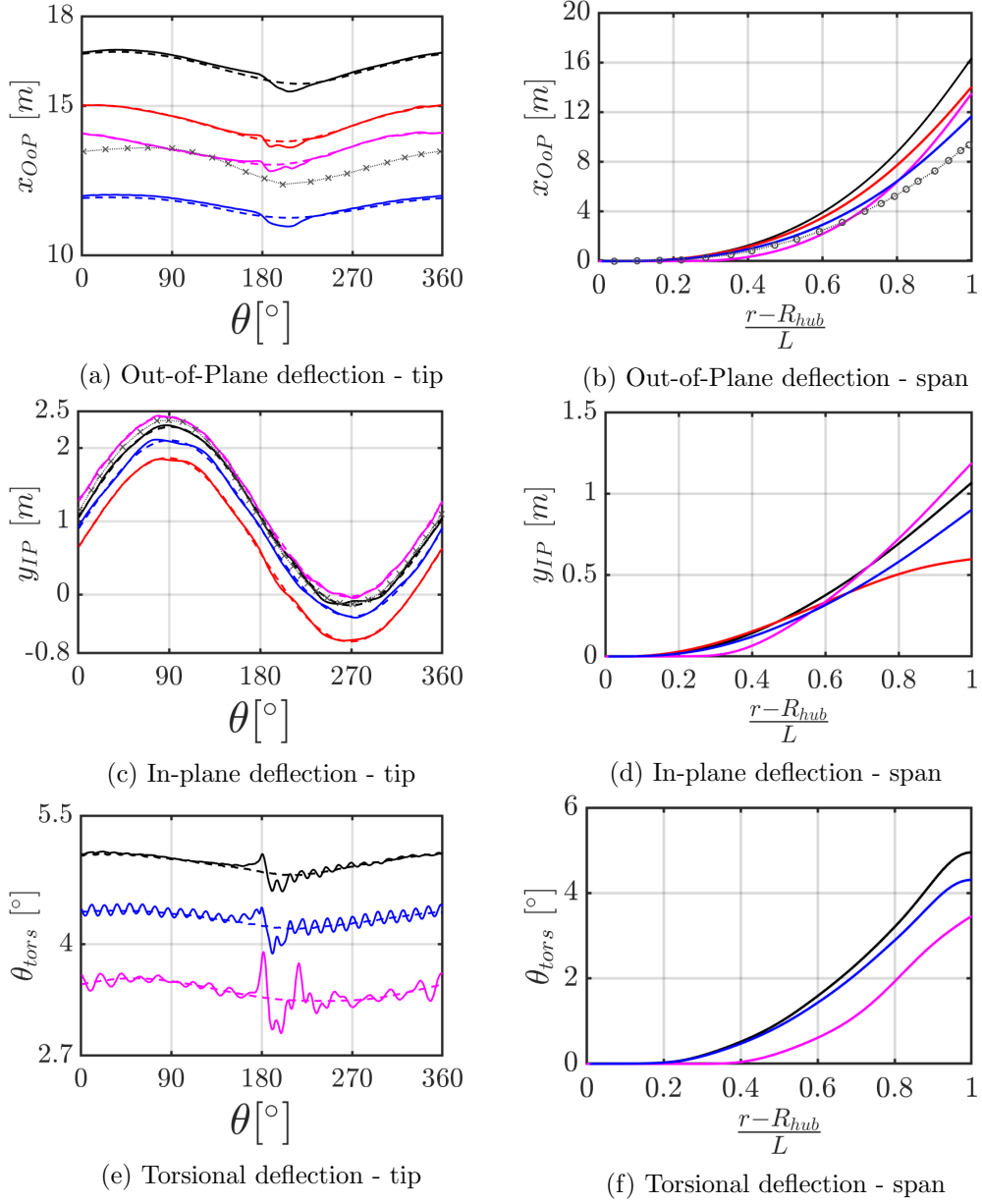
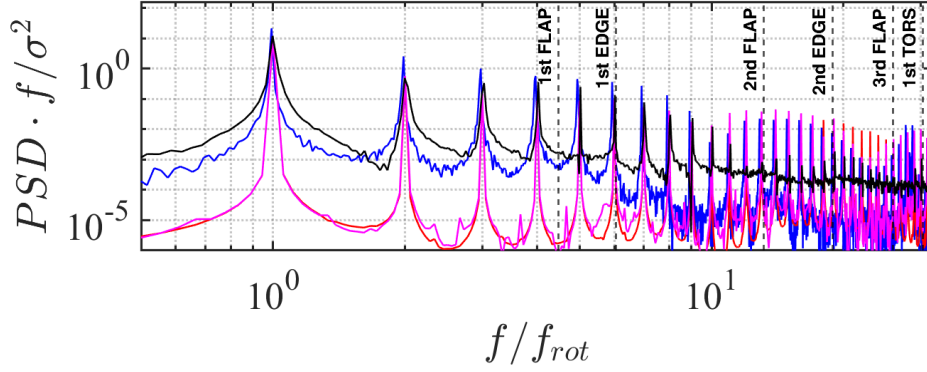
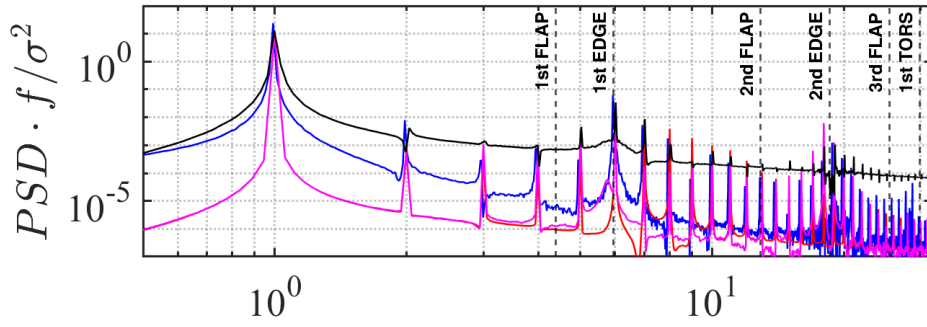


Figure 11: Phase-averaged deflections at the tip of the blade (left column) and time-averaged deflections along the blade span (right column). CFD-CSD/OV: TN —, RO ----. CFD-CSD/T: TN —, RO ----. *ElastoDyn*: TN —, RO ----. *BeamDyn*: TN —, RO ----. From figure 13 of Pagamonci et al. (2023) \circ , and figure 7a and 7b of Trigaux et al. (2024) \times .

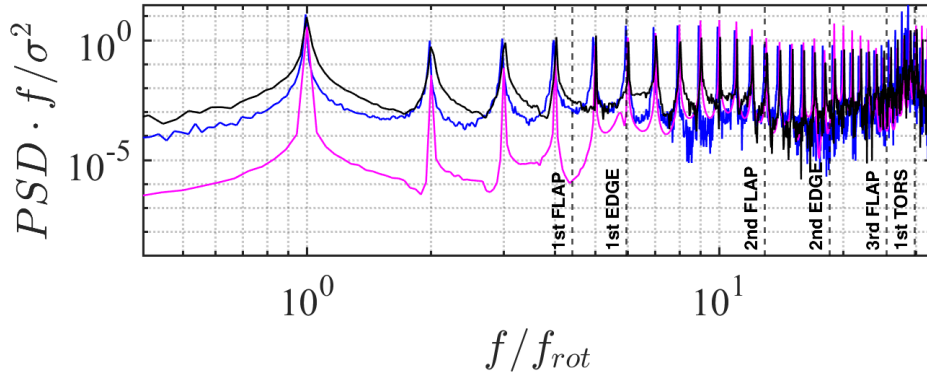
555 percentual gap of *BeamDyn* reaches 29% for the CSD-CFD/OV, and 24% for the CFD-CSD/T. It is
 556 noteworthy that the lower torsional deformation resulting from *BeamDyn* leads to the higher aerody-



(a) X_{OoP}



(b) y_{IP}



(c) θ_{tors}

Figure 12: Power Spectral Density (PSD) of the out-of-plane (a), in-plane (b), and torsional (c) deformations of the blade. The vertical dashed lines represent the first 8 eigenfrequencies of the system. CFD-CSD/OV —, CFD-CSD/T —, *ElastoDyn* —, *BeamDyn* —.

557 namic loads observed in figure 7c.

558 Finally, figure 12 illustrates the Power Spectral Density (PSD) of the blade's tip deformation compo-
 559 nents for the TN configuration (which is characterized by more complex fluid-structure interactions).
 560 The premultiplied PSD values are normalized by the variance of the signal, σ^2 , and plotted versus the

561 frequency normalized by the rotor frequency, f/f_{rot} . Spectral results have been corroborated through
562 use of the Welch and Lomb-Scargle PSD estimation algorithms.

563 Figure 12a shows the out-of-plane deformation, which we showed to be influenced mostly by the
564 aerodynamic loading. The results indicate that, for all the numerical approaches used, the observed
565 structural response does not exhibit a peak corresponding to the first flapwise natural frequency,
566 suggesting that the intrinsic dynamics of the structure might play a less prominent role in the de-
567 formation process. A similar behavior is found in the results of Trigaux et al. (2024) (see figure 6
568 of the cited paper) for the same turbine and similar inflow conditions. Noticeably, all the numerical
569 models recovered peaks at frequencies close to the (highly damped) second and third flapwise natural
570 frequencies, but they appear to rather correspond to the 13th and 26th multiple of the rotational fre-
571 quency (i.e., 13p and 26p). Both CFD-CSD solvers predict larger amplitude responses across a broad
572 frequency range compared to OpenFAST, indicating a higher capability to capture complex flow inter-
573 actions, including turbulence-induced vibrations. This effect is particularly pronounced at the lower
574 frequencies, probably due to the large-scale three-dimensional structure of the flow impinging on the
575 turbine, which is not captured by OpenFAST, also due to the fact that the impinging flow on the
576 turbine is purely two-dimensional, while it is not for CFD. For this reason, these aspects seem to be
577 under-represented in the *ElastoDyn* and *BeamDyn* solutions. Although the *ElastoDyn* curve aligns
578 with both the CFD-CSD solvers at some key frequency peaks, it does not account for the fine-scale
579 flow-structure interactions. On the other hand, the *BeamDyn* curve provides better agreement with
580 the CFD-CSD solvers, especially at higher frequencies near the blade’s natural modes, suggesting that
581 *BeamDyn* captures more of the structural dynamics, particularly the aeroelastic response, probably
582 due to its nonlinearity or to the number of degrees of freedom considered. Figure 12b shows the
583 in-plane deformation, which is primarily influenced by gravity, centrifugal, and Coriolis forces acting
584 on the blade. The CFD-CSD solvers again demonstrate stronger low-frequency components.

585 Figure 12c presents the torsional deformation for the CFD-CSD/T and *BeamDyn* solvers, excluding
586 *ElastoDyn*, which neglects the torsional DoF in the model. Additionally, also this quantity demon-
587 strates that the CFD-CSD curves predict higher amplitudes at low frequencies. However, a good
588 agreement between the two solvers is evident at higher frequencies, especially in the range around the
589 first torsional eigenfrequency.

590 5 Conclusions

591 This study investigated the aeroelastic response of the IEA 15-MW wind turbine by employing a
592 high-fidelity Computational Fluid Dynamics (CFD) solver that couples Large-Eddy Simulation (LES)
593 with a Computational Structural Dynamics (CSD) solver. Two different CSD solvers are considered:
594 the CFD-CSD/OV solver, in which the only structural quantity contributing to the definition of the
595 angle of attack is the deformation velocity, and the CFD-CSD/T solver, in which the instantaneous
596 torsional deformation is also considered when defining the local effective incidence. The results of the
597 two CFD-CSD solvers are compared with those of traditional engineering solvers such as *BeamDyn*
598 and *ElastoDyn*, both relying on Blade Element Momentum (BEM) theory. Two case studies were
599 examined: a rotor-only configuration (RO) and one that included the tower and nacelle (TN).
600 The Power Spectral Density (PSD) of the power and thrust coefficients revealed that the CFD-CSD

601 solver captures a broader range of flow-structure interactions, with a more broadband low-frequency
602 response, compared to the BEM-based solvers. The isolated low-frequency peaks found in *BeamDyn*
603 and *ElastoDyn* suggest that these solvers tend to over-simplify the aerodynamic fluctuations associ-
604 ated with phenomena such as wind shear and tower shadowing. For the large IEA 15-MW turbine,
605 the performance drop caused by tower passage is not very pronounced and the resulting oscillations
606 predicted by the BEM approach appear to be larger than the CFD-CSD solver.

607 Concerning the forces on the blade and the incidence angle, one can observe a rather good match
608 between the CFD-CSD/OV solver and *ElastoDyn*, as well as between the CFD-CSD/T model and
609 the *BeamDyn* solver. This is likely due to the presence – or not – of the torsional feedback, while
610 non-linearities of the structural solver appear to have only a limited impact on the observed quanti-
611 ties. In agreement with previous studies, the results thus suggest that including the torsional degree
612 of freedom in the structural solver is crucial for accurately describing the amplitude and dynamical
613 behaviour of the aerodynamic quantities.

614 Moreover, it is observed that duly taking into account the torsional degree of freedom reduces the
615 value of C_p . This feature is consistently observed by both CFD and BEM approaches. However, one
616 can observe that *BeamDyn* predicts lower values of the torsional deformation and thus higher values
617 of the aerodynamic edgewise forces with respect to the CFD-CSD/T approach, leading to a larger C_p
618 value than that predicted by LES. All in all, it can be concluded that for the considered setup, the
619 CFD-CSD solvers tend to exhibit larger amplitudes at lower frequencies with respect to BEM ones.

620 The structural response of the wind turbine blade has been assessed by comparing the out-of-plane, in-
621 plane, and torsional deformations obtained from the CFD-CSD solvers, *ElastoDyn*-based, and *Beam-*
622 *Dyn*-based OpenFAST solver. In-plane deformation, influenced significantly by centrifugal forces,
623 appears to be better captured by the CFD-CSD solvers, especially in the low-frequency range. Con-
624 cerning the out-of plane deflection, large discrepancies are seen between the two CFD-CSD solvers, as
625 well as between both BEM modules and the LES.

626 Our results underscore the importance of incorporating torsional deformation effects in the definition
627 of the angle of attack and using high-fidelity aeroelastic models to ensure accurate predictions of wind
628 turbine blade performance with a richer fluid dynamics. Whereas, the linearity of the structural model
629 does not appear to have a strong effect on the aerodynamical quantities, deformations and loads. In
630 general, the comparison of the results of the CFD-CSD solver with those of the engineering solver
631 shows differences especially in the region behind the tower. The observed differences likely stem from
632 the combined effects of differences in aerodynamic and structural fidelity, and cannot be uniquely
633 attributed to one component alone.

634 Future work will explore the effect of turbulent fluctuations at the inlet to better investigate the impact
635 of the atmospheric boundary layer on the aerodynamic forces, loads and deformations of the present
636 turbine.

637 **A Appendix A. Grid convergence study for LES**

638 A grid convergence study was conducted to evaluate the sensitivity of the LES results to spatial and
639 temporal resolution. Two further simulations were carried out using grids of different densities: a
640 coarser mesh and a finer mesh, having approximately 40% less and more grid points than the former

641 in each spatial direction, respectively. This allowed for a more detailed resolution of flow structures
642 and aerodynamic quantities. Moreover, both simulations use the same $CFL = 0.65$ as the present grid.
643 The average time step obtained and the other key parameters of different LES runs are summarized
644 in Table A1.

Parameter	Coarse Grid	Present Grid	Fine Grid
Total number of cells	1.31×10^8	5.37×10^8	1.36×10^9
Largest cell diagonal (m)	8.1	5.0	3.5
Smallest cell diagonal (m)	3.9	2.5	1.7
Actuator points per blade	54	86	128
Average time step (s)	0.043	0.024	0.012
Total number of threads	320	512	768

Table A1: Comparison of the main parameters for different meshes.

645 The comparison in figure A1 shows that the results obtained using the coarse and fine grids are
646 extremely close to each other along the entire blade span. In particular, the curves of the angle of
647 attack are almost indistinguishable for the coarser and the reference grid, even in the outer portion of
648 the blade, where stronger differences were expected due to tip effects and local three-dimensionality.
649 Slightly larger differences are recovered between the reference and the finer grid, but only at low
650 radius. In particular, for these two grids the maximum deviation of the incidence angle α between
651 the two simulations at 80% of the span reaches a value of $\Delta\alpha_{max} \approx 0.2^\circ$, corresponding to a relative
652 difference of 1.6%. Whereas, the maximum deviation between the reference and the coarser grids at
653 80% of the blade span is $\Delta\alpha_{max} \approx 0.1^\circ$, corresponding to a relative difference of 1.5%. Similarly,
654 the aerodynamic forces component distributions exhibit negligible variation between the reference and
655 finer resolutions, and less than 1% relative variations between the reference and the coarser grids,
656 confirming the overall consistency of the LES solution examined in the Sec. 4 with respect to mesh
657 refinement.

658 These results indicate that the coarse grid already accurately captures the main aerodynamic features,
659 making the use of a finer mesh unjustified given its higher computational cost and minimal accuracy
660 gain.

661 B Appendix B. Validation of the structural model

662 The structural model for the IEA 15MW wind turbine has been cross-validated with many other
663 aeroelastic numerical codes within the framework of the International Energy Agency (IEA) Wind TCP
664 Task 47 TURBINIA (Schepers et al., 2025). In this IEA Task, a consortium of research institutions
665 and industrial partners benchmarked their own aeroelastic codes on the IEA 15 MW wind turbine
666 (Cacciola et al., 2025). Since we cannot report in this paper data from all these partners, we provide
667 here a preliminary study was conducted to validate the structural model prior to coupling it with the
668 CFD solver. Figure B1 shows the distributions of the structural and constructive properties along the
669 blade, which were utilized as input for the modal CSD analysis. A convergence study to determine the

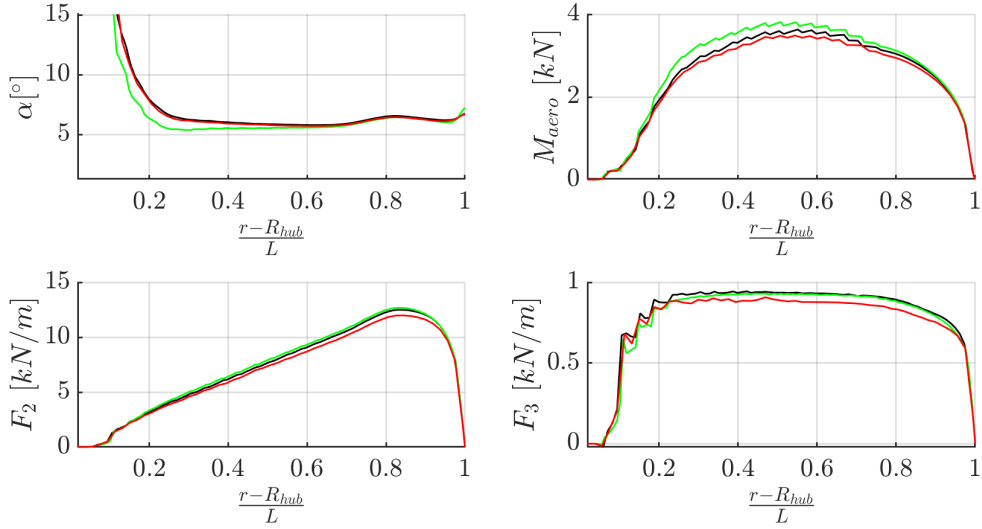


Figure A1: Average aerodynamic quantities along the blade obtained from the coarse grid (red line), the present grid (black line) and the finer grid (green line). Incidence angle (top left), Aerodynamic pitch moment (top right), flapwise aerodynamic force (bottom left), edgewise aerodynamic force (bottom right).

670 proper number of elements, N_e , (not reported here for brevity) was conducted, leading to the choice
671 $N_e = 80$. Furthermore, the results of the present structural analysis were compared with those of
672 five models including: the prismatic Timoshenko model without torsion (H2-PTNT); the Timoshenko
673 model with a fully populated stiffness matrix (H2-FPM) from the study of Rinker et al. (2020); the
674 3D Finite Element Analysis (3D FEA) selected from Zhang et al. (2023); the ElastoDyn model; the
675 BeamDyn model. Figure B2 shows the first 8 eigenfrequencies using the present method compared
676 with the results of these models. The computed values of the modal frequencies appear to be consistent
677 with the other results, although some discrepancies in the higher-order modes are observed. Moreover,
678 an analysis of the most important modes was conducted: Table B1 provides the classification of the
679 first 8 modes, whereas, Figures B3, B4, and B5 show the modal displacements for the first spanwise,
680 edgewise, and torsional modes, respectively.

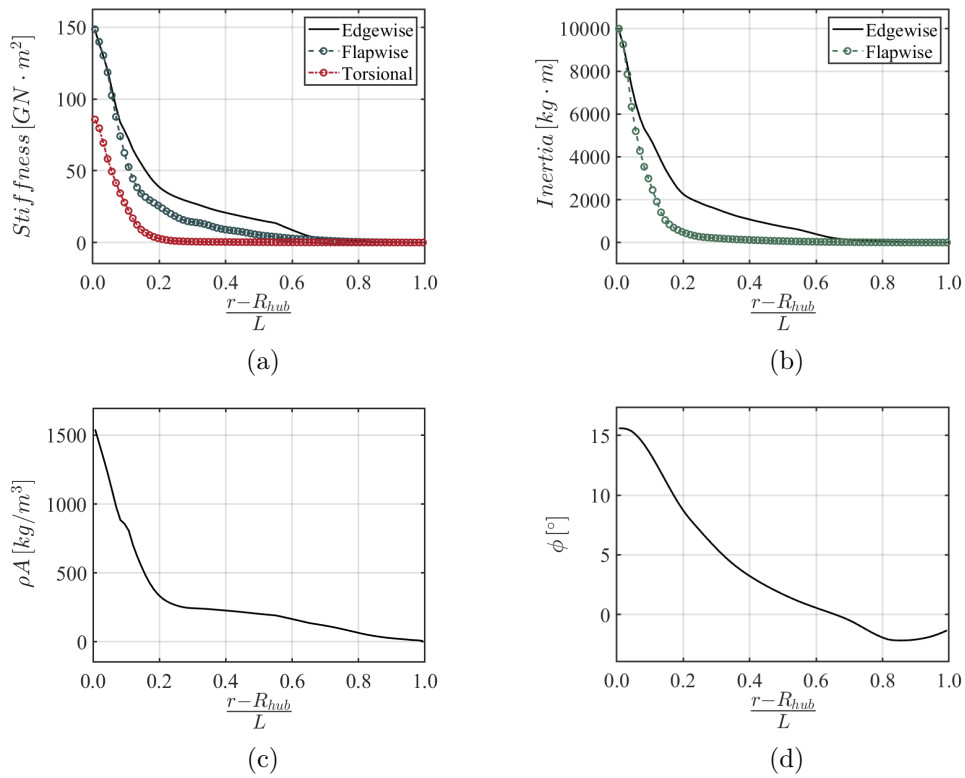


Figure B1: Structural properties of the blade along the span: (a) stiffness, (b) inertia, (c) density, (d) local twist angle.

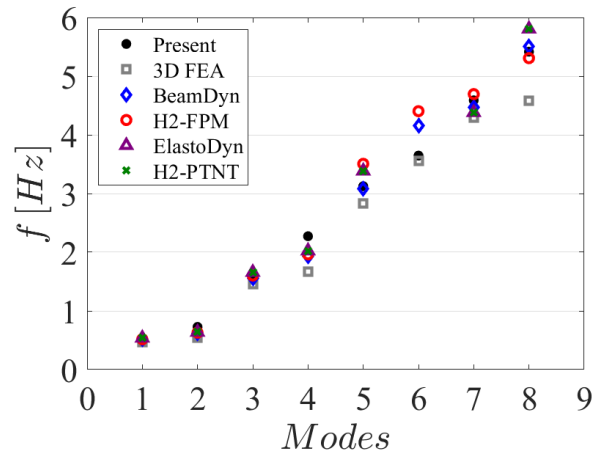


Figure B2: A comparison of the eigenfrequencies computed by different structural models.

#	$f_n[Hz]$	Mode
1	0.5369	1st flapwise
2	0.7267	1st edgewise
3	1.577	2nd flapwise
4	2.267	2nd edgewise
5	3.113	3rd flapwise
6	3.642	1st torsional
7	4.571	3rd edgewise
8	5.385	4th flapwise

Table B1: Classification of the first 8 structural modes.

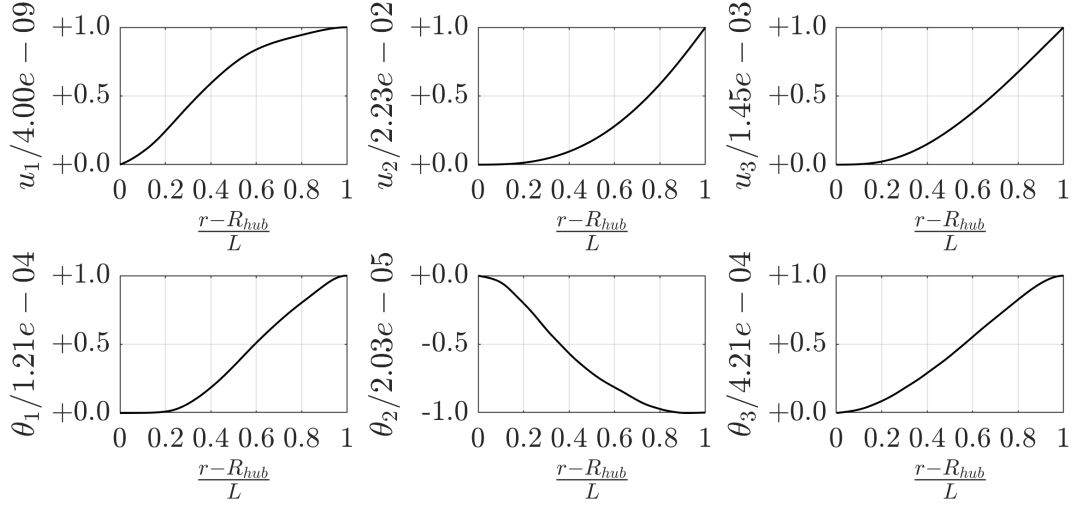


Figure B3: Mode 1 shape for all the DoFs.

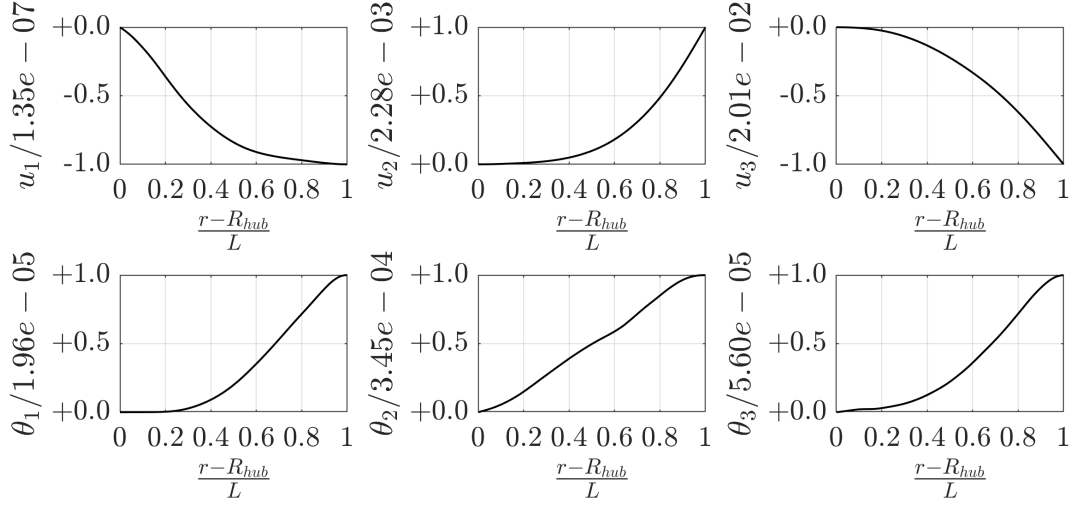


Figure B4: Mode 2 shape for all the DoFs.

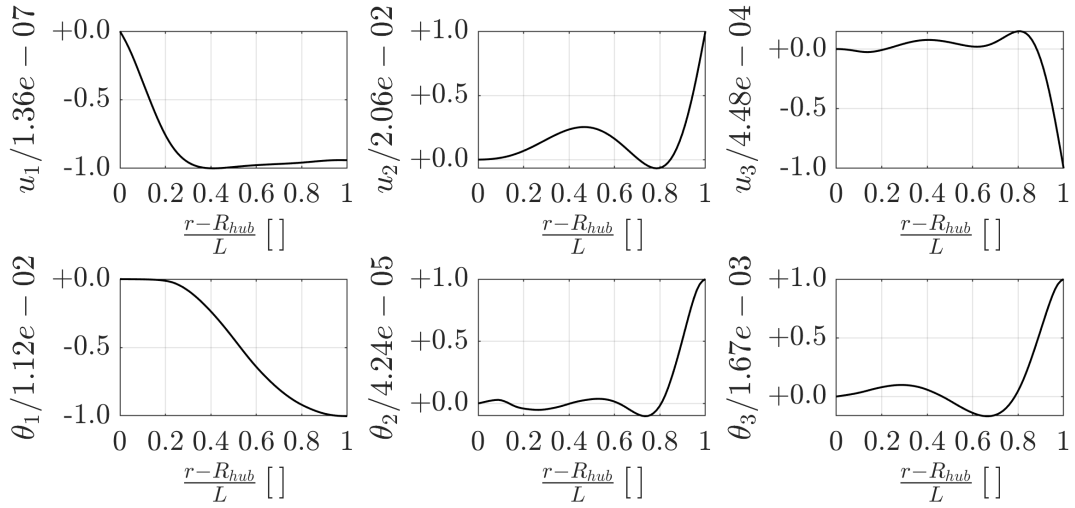


Figure B5: Mode 6 shape for all the DoFs.

681 *Author contribution.* CB: Investigation, Writing - Original draft, Formal analysis, Methodology, Soft-
682 ware, Validation. SC: Conceptualization, Investigation, Writing - Review & Editing, Supervision. FM:
683 Methodology, Software, Validation. GDP: Formal analysis, Writing - Review & Editing, Methodol-
684 ogy, software. SL: Conceptualization, Software, Supervision. PDP: Conceptualization, Investigation,
685 Writing - Review & Editing, Supervision.

686 *Competing interests.* The authors declare that they have no competing interests.

687 *Acknowledgments.* This study has been partially funded under the National Recovery and Resilience
688 Plan (NRRP), Mission 4 Component 2 Investment 1.3 - Call for tender No. 1561 of 11.10.2022
689 Project code PE0000021, Project title "Network 4 Energy Sustainable Transition – NEST", and
690 under the PRIN grant 20229YJP33, "Diffuser augmented Wind Turbines for URBban environments"
691 (DWTURB). Both are grants of Ministero dell'Università e della Ricerca (MUR), funded by the
692 European Union – NextGenerationEU. The cooperative work on the 15MW NREL wind turbine within
693 the IEA WIND TASK 47 - TURBINIA is also acknowledged. We acknowledge ISCRA for awarding
694 this project access to the LEONARDO supercomputer, owned by the EuroHPC Joint Undertaking,
695 hosted by CINECA (Italy) .

696 **References**

- 697 Abdel Hafeez, M. M. and El-Badawy, A. A.: Flutter limit investigation for a horizontal axis wind tur-
698 bine blade, *Journal of Vibration and Acoustics*, 140, 041 014, doi:<https://doi.org/10.1115/1.4039402>,
699 2018.
- 700 Allah, V. A. and Sha ei Mayam, M. H.: Large Eddy Simulation of flow around a single and two in-line
701 horizontal-axis wind turbines, *Energy*, 121, 533–544, 2017.
- 702 Bartl, J. and Satran, L.: Blind test comparison of the performance and wake flow between two in-line
703 wind turbines exposed to different turbulent inflow conditions, *Wind Energy Science*, 2, 55–76, 2017.
- 704 Bayati, I., Belloli, M., Bernini, L., and Zasso, A.: Aerodynamic design methodology for wind tunnel
705 tests of wind turbine rotors, *Journal of Wind Engineering and Industrial Aerodynamics*, 167, 217–
706 227, doi:<https://doi.org/10.1016/j.jweia.2017.05.004>, 2017.
- 707 Bazilevs, Y., Hsu, M.-C., Kiendl, J., Wüchner, R., and Bletzinger, K.-U.: 3D simulation of wind
708 turbine rotors at full scale. Part II: Fluid-structure interaction modeling with composite blades,
709 *International Journal for Numerical Methods in Fluids*, 65, 236 – 253, doi:10.1002/flid.2454, cited
710 by: 441, 2011.
- 711 Bernardi, C., Posta, G. D., Palma, P. D., Leonardi, S., Bernardoni, F., Bernardini, M., and Cherubini,
712 S.: The effect of the tower's modeling on the aero-elastic response of the NREL 5 MW wind turbine,

- 713 Journal of Physics: Conference Series, 2505, 012037, doi:10.1088/1742-6596/2505/1/012037, URL
714 <https://dx.doi.org/10.1088/1742-6596/2505/1/012037>, 2023.
- 715 Boorsma, K., Greco, L., and Bedon, G.: Rotor wake engineering models for aeroelastic applications,
716 Journal of Physics: Conference Series, 1037, 062013, doi:10.1088/1742-6596/1037/6/062013, URL
717 <https://doi.org/10.1088/1742-6596/1037/6/062013>, 2018.
- 718 Boorsma, K., Schepers, G., Aagard Madsen, H., Pirrung, G., Sørensen, N., Bangga, G., Imiela,
719 M., Grinderslev, C., Meyer Forsting, A., Shen, W. Z., Croce, A., Cacciola, S., Schaffarczyk,
720 A. P., Lobo, B., Blondel, F., Gilbert, P., Boisard, R., Höning, L., Greco, L., Testa, C.,
721 Branlard, E., Jonkman, J., and Vijayakumar, G.: Progress in the validation of rotor aerody-
722 namic codes using field data, Wind Energy Science, 8, 211–230, doi:10.5194/wes-8-211-2023, URL
723 <https://wes.copernicus.org/articles/8/211/2023/>, 2023.
- 724 Boorsma, K., Schepers, J. G., Pirrung, G. R., Madsen, H. A., Sørensen, N. N., Grinderslev,
725 C., Bangga, G., Imiela, M., Croce, A., Cacciola, S., Blondel, F., Branlard, E., and Jonkman,
726 J.: Challenges in Rotor Aerodynamic Modeling for Non-Uniform Inflow Conditions, Jour-
727 nal of Physics: Conference Series, 2767, 022006, doi:10.1088/1742-6596/2767/2/022006, URL
728 <https://doi.org/10.1088/1742-6596/2767/2/022006>, 2024.
- 729 Burton, T., Jenkins, N., Sharpe, D., and Bossanyi, E.: Wind energy handbook, John Wiley & Sons,
730 2011.
- 731 Cacciola, S., Croce, A., Bangga, G., Pirrung, G., H., M., Sørensen, N., Grinderslev, G., Bonfils, N.,
732 Persent, E., Gilbert, I., Joulin, A., Greco, L., Aryan, N., Castorrini, A., Morici, A., Chetan, M.,
733 Jonkman, J., Branlard, E., Cherubini, S., Bernardi, C., Boorsma, K., Schepers, J. D., Bianchini,
734 A., Pagamoci, L., Papi, F., Hach, O., Imiela, M., and Witt, D.: A Comparative Study of Different
735 Modeling Tools and Analysis Techniques for Aeroelastic Stability Assessment, in: submitted to The
736 Science of Making Torque from Wind, 2025.
- 737 Chen, X.: Experimental investigation on structural collapse of a large composite wind tur-
738 bine blade under combined bending and torsion, Composite Structures, 160, 435–445, doi:
739 <https://doi.org/10.1016/j.renene.2022.08.113>, 2017.
- 740 Chung, J. and Hulbert, G. M.: A Time Integration Algorithm for Structural Dynamics With Improved
741 Numerical Dissipation: The Generalized- α Method, Journal of Applied Mechanics, 60, 371–375, doi:
742 [10.1115/1.2900803](https://doi.org/10.1115/1.2900803), URL <https://doi.org/10.1115/1.2900803>, 1993.
- 743 Ciri, U., Petrolo, G., Salvetti, M. V., and Leonardi, S.: Large-Eddy Simulations of Two In-Line
744 Turbines in a Wind Tunnel with Different Inflow Conditions, Energies, 10, 821, 2017.
- 745 Courant, R., Friedrichs, K., and Lewy, H.: On the partial difference equations of mathematical physics,
746 IBM journal of Research and Development, 11, 215–234, doi:<https://doi.org/10.1147/rd.112.0215>,
747 1967.

- 748 Damgaard, M., Ibsen, L. B., Andersen, L. V., and Andersen, J. K.: Cross-wind modal properties of
749 offshore wind turbines identified by full scale testing, *Journal of Wind Engineering and Industrial*
750 *Aerodynamics*, 116, 94–108, doi:<https://doi.org/10.1016/j.jweia.2013.03.003>, 2013.
- 751 Damiani, R., Jonkman, J., and Hayman, G.: SubDyn user’s guide and theory manual, Tech. rep.,
752 National Renewable Energy Lab.(NREL), Golden, CO (United States), 2015.
- 753 Della Posta, G., Leonardi, S., and Bernardini, M.: A two-way coupling method for the
754 study of aeroelastic effects in large wind turbines, *Renewable Energy*, 190, 971–992, doi:
755 <https://doi.org/10.1016/j.renene.2022.03.158>, 2022.
- 756 Della Posta, G., Leonardi, S., and Bernardini, M.: Large eddy simulations of a utility-scale horizontal
757 axis wind turbine including unsteady aerodynamics and fluid-structure interaction modelling, *Wind*
758 *Energy*, 26, 98–125, doi:<https://doi.org/10.1002/we.2789>, 2023.
- 759 Dong, X., Lian, J., Wang, H., Yu, T., and Zhao, Y.: Structural vibration monitoring and opera-
760 tional modal analysis of offshore wind turbine structure, *Ocean Engineering*, 150, 280–297, doi:
761 <https://doi.org/10.1016/j.oceaneng.2017.12.052>, 2018.
- 762 Gaertner, E., Rinker, J., Sethuraman, L., Zahle, F., Anderson, B., Barter, G., Abbas, N., Meng, F.,
763 Bortolotti, P., Skrzypinski, W., Scott, G., Feil, R., Bredmose, H., Dykes, K., Shields, M., Allen, C.,
764 and Viselli, A.: Definition of the IEA 15-Megawatt Offshore Reference Wind Turbine, Tech. rep.,
765 International Energy Agency, URL <https://www.nrel.gov/docs/fy20osti/75698.pdf>, 2020a.
- 766 Gaertner, E., Rinker, J., Sethuraman, L., Zahle, F., Anderson, B., Barter, G., Abbas, N., Meng, F.,
767 Bortolotti, P., Skrzypinski, W., et al.: Definition of the IEA 15-megawatt offshore reference wind
768 turbine, 2020b.
- 769 Hansen, M.: *Aerodynamics of wind turbines*, Routledge, 2015.
- 770 Hansen, M. H.: Aeroelastic instability problems for wind turbines, *Wind Energy: An International*
771 *Journal for Progress and Applications in Wind Power Conversion Technology*, 10, 551–577, doi:
772 <https://doi.org/10.1002/we.242>, 2007.
- 773 Heinz, J.: *Partitioned Fluid-Structure Interaction for Full Rotor Computations Using CFD*, Ph.D.
774 thesis, Denmark, 2013.
- 775 Jonkman, J.: The New Modularization Framework for the FAST Wind Turbine CAE Tool, doi:
776 [10.2514/6.2013-202](https://arc.aiaa.org/doi/abs/10.2514/6.2013-202), URL <https://arc.aiaa.org/doi/abs/10.2514/6.2013-202>, 2013.
- 777 Jonkman, J. M., Hayman, G., Jonkman, B., Damiani, R., and Murray, R.: *AeroDyn v15 user’s guide*
778 *and theory manual*, NREL Draft Report, 46, 2015.
- 779 Krogstad, P.-A., Satran, L., and Adaramola, M. S.: Blind Test 3: calculations of the performance
780 and wake development behind two in-line and offset model wind turbines, *Journal of Fluids and*
781 *Structures*, 52, 65–80, 2015.

- 782 Manwell, J. F., McGowan, J. G., and Rogers, A. L.: Wind energy explained: theory, design and
783 application, John Wiley & Sons, 2010.
- 784 Martinez-Tossas, L. A., Churchfield, M. J., Yilmaz, A. E., Sarlak, H., Johnson, P. L., Sørensen, J. N.,
785 Meyers, J., and Meneveau, C.: Comparison of four large-eddy simulation research codes and effects
786 of model coefficient and inflow turbulence in actuator-line-based wind turbine modeling, *Journal of*
787 *Renewable and Sustainable Energy*, 10, doi:<https://doi.org/10.1063/1.5004710>, 2018.
- 788 Moeller, T.: Blade cracks signal new stress problem, *WindPower Monthly*, 25, 1997.
- 789 Moriarty, P. J. and Hansen, A. C.: *AeroDyn Theory Manual*, doi:10.2172/15014831, 2005.
- 790 Orlandi, P.: *Fluid flow phenomena: a numerical toolkit*, vol. 55, Springer Science & Business Media,
791 2012.
- 792 Orlandi, P. and Leonardi, S.: DNS of turbulent channel flows with two-and three-dimensional rough-
793 ness, *Journal of Turbulence*, p. N73, doi:<https://doi.org/10.1080/14685240600827526>, 2006.
- 794 Pagamonci, L., Papi, F., Balduzzi, F., Xie, S., Sadique, J., Scienza, P., and Bianchini, A.: To what
795 extent is aeroelasticity impacting multi-megawatt wind turbine upscaling? A critical assessment,
796 in: *Journal of Physics: Conference Series*, vol. 2648, p. 012005, IOP Publishing, doi:10.1088/1742-
797 6596/2648/1/012005, 2023.
- 798 Pino Martín, M., Piomelli, U., and Candler, G. V.: Subgrid-scale models for compressible large-eddy
799 simulations, *Theoretical and Computational Fluid Dynamics*, 13, 361–376, 2000.
- 800 Porte-Agel, F. and Wu, Y.-T.: Large-Eddy Simulation of Wind-Turbine Wakes: Evaluation of Turbine
801 Parametrisations, *Boundary Layer Meteorology*, 138, 345–366, 2011.
- 802 Reschke, C.: Flight loads analysis with inertially coupled equations of motion, in: *AIAA Atmospheric*
803 *Flight Mechanics Conference and Exhibit*, p. 6026, doi:<https://doi.org/10.2514/6.2005-6026>, 2005.
- 804 Ribeiro, A. F. P., Casalino, D., and Ferreira, C. S.: Nonlinear inviscid aerodynamics of a wind turbine
805 rotor in surge, sway, and yaw motions using a free-wake panel method, *Wind Energy Science*, 8, 661–
806 675, doi:10.5194/wes-8-661-2023, URL <https://wes.copernicus.org/articles/8/661/2023/>,
807 2023.
- 808 Rinker, J., Gaertner, E., Zahle, F., Skrzypiński, W., Abbas, N., Bredmose, H., Barter, G., and
809 Dykes, K.: Comparison of loads from HAWC2 and OpenFAST for the IEA Wind 15 MW Reference
810 Wind Turbine, in: *Journal of Physics: Conference Series*, vol. 1618, p. 052052, IOP Publishing,
811 doi:10.1088/1742-6596/1618/5/052052, 2020.
- 812 Sabale, A. K. and Gopal, N. K. V.: Nonlinear Aeroelastic Analysis of Large Wind Turbines
813 Under Turbulent Wind Conditions, *AIAA Journal*, 57, 4416–4432, doi:10.2514/1.J057404, URL
814 <https://doi.org/10.2514/1.J057404>, 2019.

- 815 Saltari, F., Riso, C., Matteis, G. D., and Mastroddi, F.: Finite-element-based modeling for
816 flight dynamics and aeroelasticity of flexible aircraft, *Journal of Aircraft*, 54, 2350–2366, doi:
817 <https://doi.org/10.2514/1.C034159>, 2017.
- 818 Santoni, C., Ciri, U., Rotea, M., and Leonardi, S.: Development of a high fidelity CFD code
819 for wind farm control, in: 2015 American Control Conference (ACC), pp. 1715–1720, doi:
820 10.1109/ACC.2015.7170980, 2015.
- 821 Santoni, C., Carrasquillo, K., Arenas-Navarro, I., and Leonardi, S.: Effect of tower and nacelle on the
822 flow past a wind turbine, *Wind Energy*, 20, 1927–1939, doi:<https://doi.org/10.1002/we.2130>, 2017.
- 823 Santoni, C., García-Cartagena, E. J., Ciri, U., Zhan, L., Valerio Iungo, G., and Leonardi, S.: One-
824 way mesoscale-microscale coupling for simulating a wind farm in North Texas: Assessment against
825 SCADA and LiDAR data, *Wind Energy*, 23, 691–710, doi:<https://doi.org/10.1002/we.2452>, 2020.
- 826 Schepers, J., Boorsma, K., Madsen, H., Pirrung, G., Bangga, G., Guma, G., Lutz, T., Potentier, T.,
827 Braud, C., Guilmineau, E., Croce, A., Cacciola, S., Schaffarczyk, A. P., Lobo, B. A., Ivanell, S., As-
828 muth, H., Bertagnolio, F., Sørensen, N., Shen, W. Z., Grinderslev, C., Forsting, A. M., Blondel, F.,
829 Bozonnet, P., Boisard, R., Yassin, K., Hoening, L., Stoevesandt, B., Imiela, M., Greco, L., Testa, C.,
830 Magionesi, F., Vijayakumar, G., Ananthan, S., Sprague, M. A., Branlard, E., Jonkman, J., Carrion,
831 M., Parkinson, S., and Cicirello, E.: IEA Wind TCP Task 29, Phase IV: Detailed Aerodynamics of
832 Wind Turbines, doi:10.5281/zenodo.4813068, URL <https://doi.org/10.5281/zenodo.4813068>,
833 2021.
- 834 Schepers, J. G., Boorsma, K., Bois, R., Bangga, G., Jonkman, J., Kelley, C., Branlard, E.,
835 Gonçalves Pinto, W., Imiela, M., Hach, O., Greco, L., Testa, C., Aryan, N., Madsen, H., Croce, A.,
836 Cacciola, S., Pirrung, G., Sørensen, N., Grinderslev, C., Bernardi, C., Cherubini, S., Bianchini, A.,
837 Papi, F., Pagamonci, L., Braud, C., Höning, L., Theron, J., and Mohan, K.: Turbinia, turbulent
838 inflow innovative aerodynamics, Tech. rep., IEA Wind TCP–Task47, 2025.
- 839 Shen, W. Z., Mikkelsen, R., Sørensen, J. N., and Bak, C.: Tip loss corrections for wind turbine
840 computations, *Wind Energy: An International Journal for Progress and Applications in Wind*
841 *Power Conversion Technology*, 8, 457–475, doi:<https://doi.org/10.1002/we.153>, 2005.
- 842 Sorensen, J. and Shen, W. Z.: Numerical Modeling of Wind Turbine Wakes, *Journal of Fluids Engi-*
843 *neering*, 124, 393–399, doi:10.1115/1.1471361, URL <https://doi.org/10.1115/1.1471361>, 2002.
- 844 Sørensen, J. N.: Aerodynamic aspects of wind energy conversion, *Annual Review of Fluid Mechanics*,
845 43, 427–448, doi:<https://doi.org/10.1146/annurev-fluid-122109-160801>, 2011.
- 846 Stevens, R. J., Martinez-Tossas, L. A., and Meneveau, C.: Comparison of wind farm large eddy
847 simulations using actuator disk and actuator line models with wind tunnel experiments, *Renewable*
848 *Energy*, 116, 470–478, 2018.
- 849 Trigaux, F., Chatelain, P., and Winckelmans, G.: Investigation of blade flexibility effects on the loads
850 and wake of a 15 MW wind turbine using a flexible actuator line method, *Wind Energy Science*, 9,
851 1765–1789, doi:<https://doi.org/10.5194/wes-9-1765-2024>, 2024.

- 852 Troldborg, N.: Actuator line modeling of wind turbine wakes, Ph.D. thesis, Technical University of
853 Denmark, 2009.
- 854 Vermeer, L., Sørensen, J. N., and Crespo, A.: Wind turbine wake aerodynamics, *Progress in aerospace*
855 *sciences*, 39, 467–510, doi:[https://doi.org/10.1016/S0376-0421\(03\)00078-2](https://doi.org/10.1016/S0376-0421(03)00078-2), 2003.
- 856 Wang, L., Liu, X., and Kolios, A.: State of the art in the aeroelasticity of wind turbine
857 blades: Aeroelastic modelling, *Renewable and Sustainable Energy Reviews*, 64, 195–210, doi:
858 <https://doi.org/10.1016/j.rser.2016.06.007>, 2016a.
- 859 Wang, Q., Jonkman, J., Sprague, M., and Jonkman, B.: *Beamdyn user’s guide and theory manual*,
860 National Renewable Energy Laboratory, 2016b.
- 861 Yu, D. O. and Kwon, O. J.: Predicting wind turbine blade loads and aeroelastic response using a
862 coupled CFD-CSD method, *Renewable Energy*, 70, 184 – 196, doi:10.1016/j.renene.2014.03.033,
863 cited by: 111, 2014.
- 864 Zahle, F., Barlas, A., Lønþæk, K., Bortolotti, P., Zalkind, D., Wang, L., Labuschagne, C., Sethuraman,
865 L., and Barter, G.: Definition of the IEA Wind 22-Megawatt Offshore Reference Wind Turbine,
866 Technical University of Denmark, doi:10.11581/DTU.00000317, dTU Wind Energy Report E-0243
867 IEA Wind TCP Task 55, 2024.
- 868 Zhang, Y., Song, Y., Shen, C., and Chen, N.-Z.: Aerodynamic and structural analysis for
869 blades of a 15MW floating offshore wind turbine, *Ocean Engineering*, 287, 115785, doi:
870 <https://doi.org/10.1016/j.oceaneng.2023.115785>, 2023.
- 871 Zheng, J., Wang, N., Wan, D., and Strijhak, S.: Numerical investigations of coupled aeroelastic
872 performance of wind turbines by elastic actuator line model, *Applied Energy*, 330, 120361, doi:
873 <https://doi.org/10.1016/j.apenergy.2022.120361>, 2023.